master's thesis

Cavity ring-down spectroscopy in analytical techniques

Mathijs de Jong

LUND
UNIVERSITY

May 2012

This thesis was written in the group of Claire Vallance at the Department of Chemistry at the University of Oxford (United Kingdom) and is the result of a research project conducted in this group. It is the thesis for the master's programme 'Organizing molecular matter' at Lund University (Sweden).

Student
Mathijs de Jong

Supervisors
Claire Vallance [‡]
Cathy Rushworth [‡]

Examiner
Ulf Olsson [§]

Abstract
This thesis contains an abstract in English as well as summaries in Swedish and Dutch.

[‡] Department of Chemistry, University of Oxford

[§] Physical Chemistry, Lund University

Abstract

Cavity ring-down spectroscopy (CRDS) is a sensitive absorption spectroscopy technique, used in the detection of very weak transitions and trace species. A laser pulse is trapped in an optical cavity, in which the intensity decays exponentially. The decay is faster in the presence of an absorbing or scattering material. In this work the method is applied in two analytical techniques. In the first, a liquid chromatography detector, the evaporative light scattering detector (ELSD), was modified to include CRDS. Solutes are detected in the ELSD by measuring light scattering. The modification was successful and detection was achieved with CRDS. However, the detection limit of CRDS (1 g L^{-1}) was not better than before modification (< 1 mg L^{-1}). Reasons for the poor sensitivity were explored and the result is confirmed by calculations. The second technique to which CRDS was applied, was headspace analysis. To circumvent common problems with this spectroscopic method in liquid samples, the vapour phase of a dye in solution was probed. Not enough dye molecules were present to make detection possible, supported by calculations. In specific applications with more volatile compounds this method might be successful.

Cavity ring-down spektroskopi i analytisk-kemiska tekniker

En viktig teknik inom fysik och kemi är absorptionsspektroskopi. Med denna teknik undersöks ett materials förmåga att absorbera ljus och det är till exempel viktigt vilken färg som absorberas. Med tanke på att vitt ljus består av alla färger, är absorption av ljus ett vanligt fenomen: röd saft är röd, eftersom den absorberar blått och grönt ljus från det vita dagsljuset. Du vet även att när man späder saft bleknar den röda färgen, det beror på att det inte längre finns tillräckligt med saft kvar för att absorbera det blå och gröna ljuset.

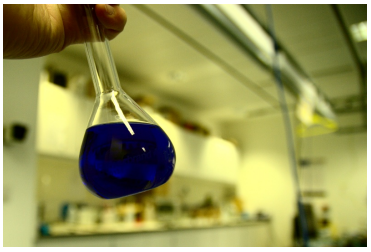

Inom kemi används detta fenomen mycket. Genom att bestämma hur mycket ljus som absorberas, är det möjligt att ta reda på hur mycket av en särskild substans det finns i en lösning. Om denna koncentration är för låg, behöver man speciella tekniker. *Cavity ring-down* spektroskopi är en metod som kan mäta absorptionen av väldigt svaga färger eller mycket utspädda lösningar. Ljuset från en laser är riktat in en så kallad kavitet. Den här kaviteten består av två speglar mellan vilka ljuset studsar fram och tillbaka. Om den absorberande lösningen nu placeras mellan speglarna, kan ljuset absorberas av lösningen.

I min avhandling har jag gjort två experiment med den här tekniken. Först används den i en detektor för kromatografi. Kromatografi är en metod för att separera olika ämnen i en blandning. Efter denna separation kommer successivt ämnena från kromatografen. En detektionsmetod behövs för att se när de olika ämnena kommer ut från kromatografen. Till exempel med en ljusspridningsdetektor detekterar man ljusspridning från det som kommer från kromatografen. Jag försökte använda cavity ring-down spektroskopi för att detektera denna spridning. Detta var faktiskt möjligt, men cavity ring-down spektroskopi kunde inte göra detta bättre än den konventionella tekniken.

I det andra experimentet försökte jag att detektera ljusabsorptionen i ångan av en färgad lösning. En kavitet byggdes upp ovanför en klarblå lösning, i hopp om att molekylerna från lösningen avdunstade i tillräckligt stor mängd för att ge absorption i kaviteten. Eftersom cavity ring-down spektroskopi ofta är svårt att utföra på vätskor, skulle detta kunna vara en bättre metod. Tyvärr avdunstade den färgglada lösningen inte tillräckligt för att detektera absorptionen i vätskans ånga.

Cavity ring-down spectroscopie toegepast op analytisch-chemische technieken

Een belangrijke techniek in de natuurkunde en scheikunde is absorptiespectroscopie. Hierbij wordt onderzocht in welke mate een materiaal licht absorbeert, waarbij bijvoorbeeld belangrijk is welke kleur wordt geabsorbeerd. In gedachten houdend dat wit licht een samenstelling is van alle kleuren, is de absorptie van licht een alledaags verschijnsel: rode limonade is rood, omdat de limonade het blauwe en groene licht absorbeert uit het witte daglicht. Je weet ook dat als de limonade verdund wordt, de rode kleur vervaagt: er is niet genoeg limonadesiroop meer om het blauwe en groene licht te absorberen.

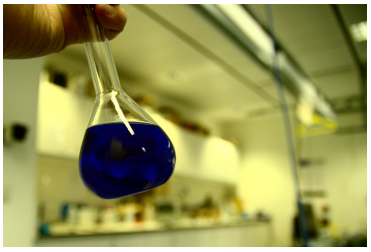

In de scheikunde wordt van dit verschijnsel dankbaar gebruik gemaakt. Door te bepalen hoeveel licht er wordt geabsorbeerd, kan men weten hoeveel van een bepaalde stof in een oplossing aanwezig is. Als de concentratie absorberende stoffen echter te laag wordt, zijn er speciale technieken nodig. *Cavity ring-down* spectroscopie is een methode die in staat is de absorptie van hele zwakke kleuren of sterk verdunde oplossingen te meten. Het licht van een laser wordt in een zogenaamde *cavity* geschenen. Deze cavity bestaat uit twee spiegels, waartussen het licht heen en weer kaatst. Als de absorberende oplossing nu tussen de spiegels wordt geplaatst, heeft het licht tijdens het heen en weer kaatsen vaak de mogelijkheid om geabsorbeerd te worden.

In mijn thesis heb ik twee experimenten gedaan met deze techniek. Eerst werd deze toegepast in een chromatografiedetector. Chromatografie is een methode om mengsels van stoffen te scheiden. Na deze scheiding komen de stoffen achtereenvolgens uit de chromatograaf en een detectiemethode is nodig om te zien wanneer de stoffen uit de chromatograaf komen. Met een verstrooiingsdetector, bijvoorbeeld, wordt gekeken of hetgeen uit de chromatograaf komt licht verstrooit. Verstrooiing is proces dat plaats kan vinden na absorptie, waarbij het licht weer wordt uitgezonden. Als dat gebeurt, weet de chemicus dat een bepaalde stof aanwezig is in het mengsel. Ik heb geprobeerd om cavity ring-down spectroscopie te gebruiken om deze verstrooiing waar te nemen. Dit bleek inderdaad mogelijk, maar cavity ring-down spectroscopie bleek niet in staat om dit beter te doen dan de conventionele techniek hiervoor.

In het tweede experiment werd getracht de absorptie van de damp van een gekleurde oplossing te detecteren. Een cavity werd gebouwd boven een felblauwe oplossing, in de hoop dat de moleculen uit de oplossing genoeg verdampten om te zorgen voor absorptie in de cavity. Omdat cavity ring-down spectroscopie vaak lastig is in vloeistoffen, zou dit een betere methode kunnen zijn. Helaas verdampte de felgekleurde oplossing niet voldoende om te zorgen voor absorptie in de damp boven de oplossing.

Contents

Chapter 1

Introduction

Absorption spectroscopy is a very powerful analytical technique, used in many fields of physics and chemistry, including molecular physics, analytical chemistry and remote sensing. Variations on the basic technique exist, but the main principle is universal: the absorption of light by a material of interest is probed at a wavelength or wavelengths of interest. In the most basic experiment, of which a schematic drawing is shown in Figure 1.1, a light beam is directed through the sample and the transmitted beam is studied by a detector. The ratio between the transmitted

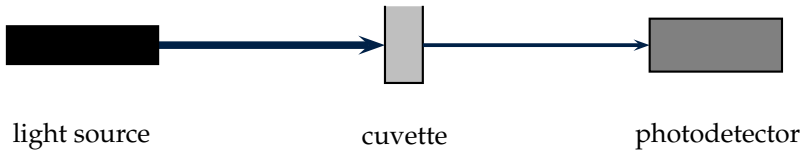

Figure 1.1: A schematic overview of a basic absorption spectroscopy experiment. A light source is directed through a cuvette with the solution of interest, after which the transmitted intensity is measured by a detector.

and incident light intensities gives information about the absorbing qualities of the material. This is quantified in the Beer-Lambert law

$$T = \frac{I(x)}{I(0)} = \exp\Big[- \sigma(\nu) N x\Big], \tag{1.1}$$

in which the transmission T is the ratio between the transmitted intensity $I(x)$ and incident intensity $I(0)$, $\sigma(\nu)$ is the frequency dependent attenuation cross section, N the number density of the attenuating material and x the path length through the material. In an experiment the ratio of intensities and the path length are known, so when either the attenuation cross section or the

number density is also known, the other can be derived from the Beer-Lambert law.

From this law it becomes clear that when absorption is weak, either because the attenuation coefficient is low, because the concentration of the substance is low or because the path length is short, absorption spectroscopy meets its limit. Only a small change in transmitted light intensity relative to the incident intensity is then observed. The smallest detectable change in intensity in an absorption measurement is determined by the stability of the light source and the attainable signal-to-noise ratio from the detector. Cavity ring-down spectroscopy (CRDS) offers a route to overcome these limitations.

Cavity ring-down spectroscopy (CRDS) is a very sensitive absorption spectroscopy technique, which was first described by O'Keefe and Deacon in 1988.[1] A schematic drawing of a CRDS experiment is shown in Figure 1.2. CRDS employs an optical cavity, for example a Fabry-Pérot cavity formed between two highly reflective concave mirrors, in which a laser beam is trapped. The laser beam, if supported by the cavity, will be reflected many times and will slowly lose power due to losses at the imperfect mirrors. The intensity of the beam in the cavity is probed as a function of time after the initial laser pulse by measuring the intensity of the light leaking from the back mirror. When an absorbing or scattering species is placed in the cavity, the decay in intensity will be faster, thus giving the possibility of measuring the attenuation coefficient. As will be shown in Chapter 2, there is a simple correlation between the decrease in decay time and the absolute attenuation coefficient, which makes CRDS a very useful technique for absorption spectroscopy.

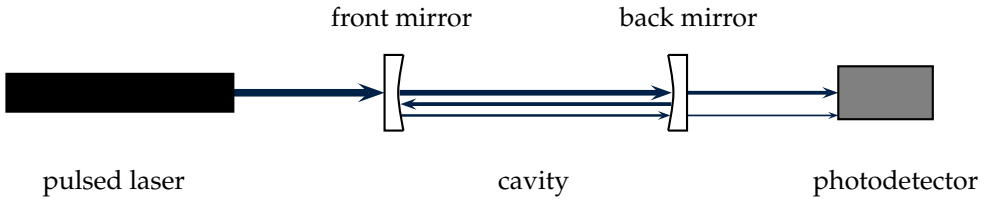

Figure 1.2: A schematic drawing of a CRDS setup. A laser beam is trapped in an optical cavity consisting of two concave mirrors, and the intensity leaking from the cavity is detected at the back of the second mirror. An absorbing or scattering sample is then placed between the mirrors and the decrease in decay time is measured.

In this thesis CRDS is applied to two analytical problems. Firstly, CRDS is explored as a means of improving the sensitivity of evaporative light scattering detection (ELSD), which is a commonly used detector in liquid chromatography. The second application is headspace absorption spectroscopy. To circumvent problems with CRDS in liquid samples, the vapour phase of a solution, the headspace, can be probed. By using CRDS on the headspace, it might be possible to probe the solutes in a solution if their vapour pressures are sufficiently high.

Chapter 2

General theory

2.1 Beer-Lambert law

As noted in Chapter 1, conventional absorption spectroscopy works by passing a light beam through the absorbing or scattering sample and comparing the intensities of the light beam before and after transmission through the sample. The absorption or scattering cross section may be calculated by using the Beer-Lambert law. The law was first described by Bouguer in 1729[2] and was later revised by Lambert and Beer.[3,4] It describes the extent to which light is attenuated when travelling through an absorbing or scattering material, and is easily derived, as follows.

It is assumed that a light beam travelling in the x-direction with intensity $I(x)$ and frequency ν is attenuated in a slab of thickness $\mathrm{d}x$ by an amount $\mathrm{d}I(x)$ and that this amount is proportional to the intensity of the beam at that point, the number density of the absorbing or scattering molecules N and the (frequency dependent) attenuation cross section $\sigma(\nu)$. This is summarised in the differential equation

$$\mathrm{d}I(x) = -\sigma(\nu)\, N\, I(x)\, \mathrm{d}x, \tag{2.1}$$

which solves to

$$I(x) = I(0) \cdot \exp\Big[-\sigma(\nu)\, N\, x\Big], \tag{2.2}$$

where $I(0)$ is the intensity of the incoming light beam before passing through the sample. The attenuation can be caused by two processes: absorption and scattering. Both cross sections

combine additively to form the attenuation cross section

$$\sigma(\nu) = \sigma_a(\nu) + \sigma_s(\nu), \tag{2.3}$$

in which $\sigma_a(\nu)$ is the absorption cross section and $\sigma_s(\nu)$ is the scattering cross section.

2.2 Photon bullet model

In CRDS a change in the decay rate of light intensity in a cavity is measured, rather than the overall change in intensity. For CRDS to be as useful as conventional absorption spectroscopy, a relation between the decrease in decay time of the signal and the attenuation cross section must be derived, the equivalent of the Beer-Lambert law for conventional absorption spectroscopy.

When a light pulse with intensity I_{in} is directed into the cavity, it initially encounters the first mirror. It is assumed that the mirror can either reflect or transmit the radiation through the first mirror, with respective probabilities of R and T, such that $R + T = 1$. After transmission through the first mirror the light travels through the cavity, where it may be absorbed or scattered by the sample, which has an attenuation cross section $\sigma(\nu)$. The probability that a photon will be transmitted through the cavity on the first pass is therefore given by the Beer-Lambert law. A fraction T of the first pulse is then transmitted through the second mirror before being detected. The detected intensity from the first pass through the cavity is

$$I_0 = I_{\text{in}} \cdot T^2 \cdot \exp\Big[-\ \sigma(\nu)\, N\, d\Big], \tag{2.4}$$

in which d is the path length through the absorbing or scattering material. After another round trip of the cavity, the intensity is decreased further by reflection at each mirror and absorption or scattering in the cavity. The remaining intensity is[5]

$$I_1 = I_0 \cdot R^2 \cdot \exp\Big[-\, 2\, \sigma(\nu)\, N\, d\Big]. \tag{2.5}$$

With every round trip the beam is attenuated by a factor $R^2 \cdot \exp\Big[-\, 2\, \sigma(\nu)\, N\, d\Big]$; thus for round trip number n the remaining intensity is[5]

$$\begin{aligned} I_n &= I_0 \cdot R^{2n} \cdot \exp\Big[-\, 2n\, \sigma(\nu)\, N\, d\Big] \\ &= I_0 \cdot \exp\Big[-\, 2n\Big(\sigma(\nu)\, N\, d - \ln R\Big)\Big]. \end{aligned} \tag{2.6}$$

This equation assumes that the pulsed laser results in resolved pulses at the detector, which is true if the light pulse is shorter than the time required for a round trip of the cavity, *i.e.*

$$t_{\text{pulse}} < \frac{2L}{c}, \tag{2.7}$$

where t_{pulse} is the laser pulse length, L is the length of the cavity, and c is the speed of light. Whether the pulses are then detected separately depends on the time resolution of the detector. In the case of resolved pulses, the equation predicts the pulse height at the peak of a pulse in the decay. In the case that the signal is detected as a continuous decay, the equation for the decaying signal can be rewritten in terms of time rather than number of passes through the cavity. Using $t = \frac{2nL}{c}$ to write t in terms of n, the intensity becomes[5]

$$I(t) = I_0 \cdot \exp\left[-\frac{tc}{L}\Big(\sigma(\nu)\, N\, d - \ln R\Big)\right]. \tag{2.8}$$

This equation makes clear that the signal shows an exponential decay as a function of time, with a decay time constant, or 'ring-down time'[6]

$$\tau = \frac{L}{c\Big(\sigma(\nu)\, N\, d - \ln R\Big)}. \tag{2.9}$$

Figure 2.1 shows both a simulation of the expected form of the detected signal if the pulses can be resolved, namely an exponentially decaying train of pulses, as well as the expected form of the detected signal in case they cannot be resolved, namely a single exponential decay.

If there is no absorbing or scattering material in the cavity ($N = 0$), Equation 2.9 reduces to

$$\tau_0 = -\frac{L}{c\, \ln R}. \tag{2.10}$$

We see that the ring-down time, τ_0, is an intrinsic property of a cavity, only depending on the length of the cavity and the reflectivity of the mirrors. The ring-down time τ_0 is the average time that a photon spends in the cavity in the absence of an absorbing or scattering species. The path length per ring-down time for a photon in the cavity can thus be calculated by using $s = c \cdot \tau_0$, in which s is the average path length of a photon in the cavity. The path length is then

$$s = -\frac{L}{\ln R}. \tag{2.11}$$

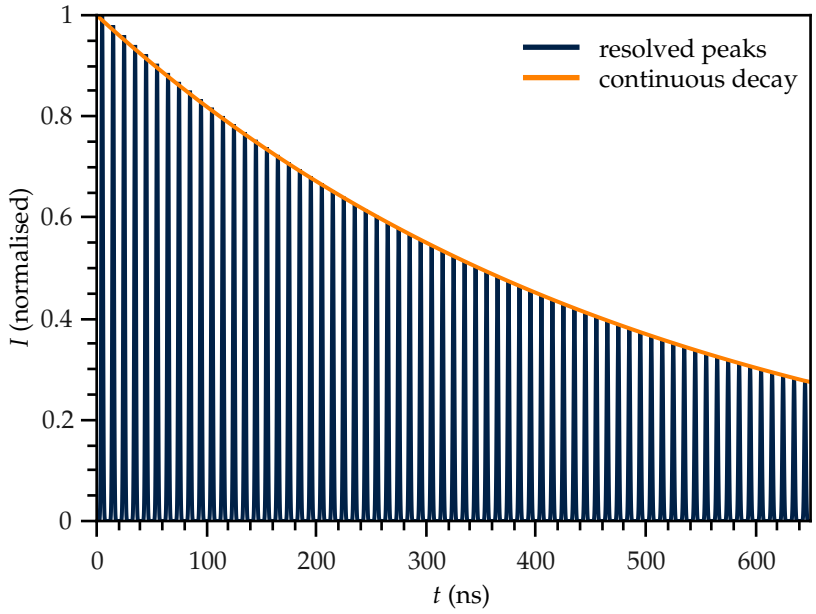

Figure 2.1: Simulation of the expected intensity pattern as a function of time in the case that the laser pulse travelling in the cavity can be resolved in separate peaks (blue line) and in case it cannot be resolved (orange line). This ring-down corresponds to an empty cavity with a length of 1.5 m and with a mirror reflectivity of 99 %.

The highly reflective mirrors used in CRDS measurements typically have $R \approx 99.99\,\%$. This reveals the first advantage of CRDS over conventional absorption spectroscopy. It follows from Equation 2.11 that the path length in a typical one meter cavity can be up to a kilometre or more. Compared to conventional absorption spectroscopy, with a path length of a few centimetres, this provides a huge enhancement in sensitivity.

To obtain an expression for the attenuation cross section in terms of the decay times with and without the absorbing species, the equations for τ and τ_0 can be combined into

$$\frac{1}{\tau} - \frac{1}{\tau_0} = \frac{c\,\sigma(\nu)\,N\,d}{L}, \tag{2.12}$$

which results in an expression for the attenuation cross section[7]

$$\kappa = \sigma(\nu)\,N = \frac{L}{c\,d}\,\frac{\tau_0 - \tau}{\tau_0 \tau}. \tag{2.13}$$

Conventional absorption spectroscopy is often limited in sensitivity by fluctuations in the intensity of the light source, which can make it difficult to precisely determine the intensity ratio of the

incoming and transmitted beam. Equation 2.13 reveals the second important advantage of CRDS: the measured attenuation cross section is not a function of the initial light intensity, which causes the sensitivity to be essentially independent of any intensity fluctuations in the light source (which can be significant for pulsed lasers). The sensitivity of CRDS is instead determined by the ability to carry out an accurate measurement of the ring-down time. This is not dependent on any fluctuations in the light source and can in practise be determined very precisely. The light source should be powerful enough to allow a sufficiently large signal to be detected at the cavity output in order to extract the ring-down time accurately. If this signal is too weak, the ring-down will be too noisy to achieve this. The detected intensity is a function of the laser intensity and the mirror transmission, but any fluctuation in this intensity does not influence the ring-down time determination.

To obtain an expression for the detection limit, Equation 2.13 can be used to write

$$\sigma(\nu)\, N = \frac{\ln R}{d}\left(\frac{\Delta\tau}{\tau}\right), \tag{2.14}$$

in which $\Delta\tau = \tau - \tau_0$ is the change in ring-down time which can be measured. This is determined by the signal-to-noise ratio of the ring-down measurement, and is often defined as three times the standard deviation in the baseline ring-down time. The resulting expression for the detection limit of a given experimental setup is

$$\kappa_{\min} = \Big(\sigma(\nu)\, N\Big)_{\min} = \frac{\ln R}{d}\left(\frac{\Delta\tau}{\tau}\right)_{\min}. \tag{2.15}$$

This equation shows that the detection limit in a specific experimental setup is determined by the precision with which the decrease in ring-down time can be measured. It also shows that with a longer path length through the sample and higher reflectivity mirrors the detection limit will improve.

2.3 Cavity enhanced absorption spectroscopy

A variation on CRDS is cavity enhanced absorption spectroscopy (CEAS). This method operates with the same experimental setup as CRDS, but for CEAS the integrated intensity from the cavity is measured, rather than the decay time of the intensity. When an exponentially decaying signal $I(t) = I_0 \cdot \exp\left[-\frac{t}{\tau}\right]$ is integrated, the result is

$$Y = \int_0^\infty I(t)\,\mathrm{d}t = \int_0^\infty I_0 \cdot \exp\left[-\frac{t}{\tau}\right]\mathrm{d}t = I_0\,\tau, \tag{2.16}$$

in which Y is the integrated intensity. Combining this with Equation 2.13, the result is[7]

$$\sigma(\nu)\, N = \frac{\ln R}{d}\left(1 - \frac{S_0}{S}\right), \tag{2.17}$$

in which S is the integrated intensity in the presence of an absorbing compound, while S_0 is the integrated intensity measured for the empty cavity. CEAS is not limited to pulsed lasers and can easily be done with continuous wave lasers. Equation 2.17 is also valid for continuous wave lasers.

One advantage of CRDS, that the signal is not dependent on fluctuations in the laser intensity, is not shared by CEAS, since Equation 2.17 clearly depends on laser intensities. Instabilities in the light source are therefore one of the limiting factors determining the detection sensitivity of a CEAS measurement.

2.4 Cavity stability

A complete description of light in a cavity treats light as a wave. Such a rigorous derivation is set out in Appendix A and the key results are summarised in this section.

When designing a cavity, in order to achieve a stable mode structure there are requirements regarding the length of the cavity and the curvature of the concave mirrors used in the cavity. For this reason it is useful to derive the requirements for the geometrical properties of the cavity.

A ring-down event is observed when a beam of light is reflected stably back and forth in a cavity. A proper description of the beam at some point z in the propagation direction can be formulated in terms of its width and the curvature of its wavefront. Both properties can be contained in a complex quantity q, the beam parameter[8]

$$\frac{1}{q(z)} = \frac{1}{R(z)} - \frac{2\,\mathrm{i}}{k\, w^2(z)}, \tag{2.18}$$

in which w is the beam width, R the radius of curvature of the wavefront and k is the wave number, given by $\frac{2\pi}{\lambda}$ in which λ is the wavelength of the light. In Appendix A it is shown that it follows from this definition that w is indeed the beam radius and R is indeed the radius of curvature of the wavefront.

When a beam propagates through an optical system (moving through free space, being reflected by a mirror, *etc.*), it can be described using ray transfer matrix analysis.[9] This means that the change in q during the propagation is described by a transformation matrix. For example, a mirror transforms a beam with complex beam parameter q_1 into a beam with complex beam

parameter q_2 according to

$$\begin{pmatrix} q_2 \\ 1 \end{pmatrix} = \begin{pmatrix} A & B \\ C & D \end{pmatrix} \begin{pmatrix} q_1 \\ 1 \end{pmatrix}. \tag{2.19}$$

The *ABCD*-matrices corresponding to a variety of optical elements and other processes can be derived and are available in literature.[9] When going through several elements or processes, the new q-value can be calculated by multiplying the corresponding matrices. The equation can also be rearranged as

$$\frac{1}{q_2} = \frac{C + D\frac{1}{q_1}}{A + B\frac{1}{q_1}}. \tag{2.20}$$

An optical cavity will support a wave when the wave is superimposed on every cycle (in wavefront curvature, beam size and phase), *i.e.* when a standing wave is formed within the cavity. For the case in which the matrix $\left(\begin{smallmatrix} A & B \\ C & D \end{smallmatrix}\right)$ represents the transformation of the beam from one position in the cavity to the same position after a round trip, it must the true that $q_2 = q_1$. In this case the matrix describes the reflection of the beam at one mirror (with radius of curvature R_1), propagation through the cavity to the second mirror, reflection at the second mirror (radius of curvature R_2) and finally propagation back through the cavity to the first mirror. The matrix for travelling through empty space (*i.e.* the cavity) of length L is

$$\begin{pmatrix} 1 & L \\ 0 & 1 \end{pmatrix} \tag{2.21}$$

and the matrix for reflection from a mirror with radius of curvature R (which is positive for a concave mirror) is

$$\begin{pmatrix} 1 & 0 \\ -\frac{2}{R} & 1 \end{pmatrix}. \tag{2.22}$$

The curvature of a mirror can also be defined by its stability parameter g. We will show later that the definition

$$g = 1 - \frac{L}{R} \tag{2.23}$$

is convenient. Now the matrix for reflection at a concave mirror can be written as

$$\begin{pmatrix} 1 & 0 \\ \frac{2g-2}{L} & 1 \end{pmatrix}. \tag{2.24}$$

The resulting matrix after one round trip in the cavity is found by multiplying the matrices of the constituent mirrors with the stability parameters g_1 and g_2 and the matrices of propagation in space

$$\begin{aligned}\begin{pmatrix} A & B \\ C & D \end{pmatrix} &= \begin{pmatrix} 1 & L \\ 0 & 1 \end{pmatrix}\begin{pmatrix} 1 & 0 \\ \frac{2g_2-2}{L} & 1 \end{pmatrix}\begin{pmatrix} 1 & L \\ 0 & 1 \end{pmatrix}\begin{pmatrix} 1 & 0 \\ \frac{2g_1-2}{L} & 1 \end{pmatrix} \\ &= \begin{pmatrix} 2g_1 - 1 + \frac{\left((2g_1-1)L+L\right)\left(2g_2-1\right)}{L} & (2g_1-1)\,L + L \\ \frac{2g_1-2}{L} + \frac{\left(2g_1-1\right)\left(2g_2-2\right)}{L} & 2g_1 - 1 \end{pmatrix},\end{aligned} \tag{2.25}$$

Using the condition $q_2 = q_1 = q$ and Equation 2.20, we obtain

$$\frac{1}{q} = \frac{\frac{2g_1-2}{L} + \frac{\left(2g_1-1\right)\left(2g_2-2\right)}{L} + (2g_1-1)\,\frac{1}{q}}{2g_1 - 1 + \frac{\left((2g_1-1)L+L\right)\left(2g_2-1\right)}{L} + \left((2g_1-1)\,L + L\right)\frac{1}{q}}. \tag{2.26}$$

Solving for $\frac{1}{q}$, the result is

$$\frac{1}{q} = \frac{g_1 - g_1g_2 \pm \mathrm{i}\sqrt{g_1g_2\,(1-g_1g_2)}}{g_1 L}. \tag{2.27}$$

A closer inspection of Equation 2.18 tells us that $\frac{1}{q}$ must have an imaginary part not equal to zero, if we do not allow an infinite beam width (which cannot be allowed for a stable beam in a cavity). For this reason Equation 2.27 must also have an imaginary part not equal to zero. Since the stability parameters g_1 and g_2 and cavity length L are real, this imposes a condition on the terms in the square root

$$g_1g_2\,(1 - g_1g_2) > 0; \tag{2.28}$$

$$0 < g_1g_2 < 1. \tag{2.29}$$

This treatment reveals that for a stable cavity, the product of the stability parameters of the two constituent mirrors of the cavity should be between 0 and 1. For a symmetrical cavity, having two concave mirrors with a radius of curvature R, this reduces, with the help of Equation 2.23, to

$$0 < L < R \qquad \text{or} \qquad R < L < 2R. \tag{2.30}$$

The cavity length can thus be in either of two regions: between 0 and R or between R and $2R$.

Chapter 3

Evaporative light scattering detection

3.1 Introduction

One of the central skills in chemistry is the art of separation. The separation of a mixture into its constituent components has been key to the discovery of many important elements and molecules. Many techniques are available to today's chemists, notably chromatography, which was discovered by the Russian Tswett in 1905[10] and was developed further over the next few decades.[11]

In the development of chromatography a crucial driving force has been, and remains, the availability of suitable detectors. The first continuous flow detector to be developed for liquid chromatography was the refractive index detector by Tiselius and Claesson in 1942.[12] Since then many more detectors have been developed, and nowadays the ultraviolet absorption detector is the most widely used detector for liquid chromatography.[12]

In this chapter, we investigate the evaporative light scattering detector (ELSD). The detector functions by evaporating the solvent of the eluate, after which the solutes which have not been evaporated are detected by measuring the intensity of the light they scatter. The advantage of this detector over the ultraviolet absorption detector is that absorption in the ultraviolet region of the spectrum is no longer a requirement. The detector is only limited by the volatility of the solutes. Any solute which is less volatile than the solvent is detected, and the versatility of the ELSD is the reason that it is also known as the mass detector.

Development of detectors with lower detection limits is desirable, since this makes the detection of compounds very low in concentration possible. In, for example, the result of an organic synthesis, this can give great insight into the performed reaction; minor side products from competing pathways can be detected and the purity of reactant and product can be verified. For this reason liquid chromatography and the ELSD are commonly used in the pharmaceutical industry. Also, more sensitive detection allows the use of smaller reaction volumes, which can be important

for health and safety, economic and environmental reasons.

The ELSD detects the scattered light by relatively simple means. A light beam from a lamp is directed through the stream of solute particles, after which the scattered light is measured with a light sensitive detector. Increasing the sensitivity of the scattered light detection will improve the detection limit. Cavity ring-down spectroscopy can be used to measure the attenuation by scattering and the aim of this project is to investigate whether the application of CRDS can be put into practice for detection in an ELSD and whether this will improve the detection limit.

3.2 Theory

3.2.1 Liquid chromatography detectors

Liquid chromatography is a powerful technique used to separate a large variety of mixtures into their constituent compounds. A chromatographic column is constantly fed with a solvent, the eluent, while at some point the mixture is brought into the column. Due to different affinities with the column, the different compounds in the mixture each move through the column with a characteristic velocity. The result is that the various components of the mixture are separated in time as they leave the column. The eluent leaving the column, usually containing a single dissolved compound at a given point in time, is called the eluate, and the presence of the solute in the eluate can be detected by a suitable detector. A short overview of the most commonly used liquid chromatography detectors is given below. The advantages and disadvantages of each technique are summarised, allowing comparison with the ELSD.

Refractive index detectors

Refractive index detection relies on measuring a change in the refractive index of the eluate as different fractions emerge from the column. The refractive index can be measured by a variety of methods, for example by measuring the refraction angle of a beam at the air-eluate surface. The angle of refraction obeys Snell's law [13]

$$n_1 \sin\theta_1 = n_2 \sin\theta_2. \tag{3.1}$$

In this equation n_1 is the refractive index of air, θ_1 the angle of incidence, n_2 the refractive index of the eluate and θ_2 the angle of refraction. A change in the angle of refraction can be measured and reflects a change in n_2. Another way of measuring the change in n_2 is by measuring the reflectance and using the Fresnel equation to relate this to the refractive index. [13] Refractive index measurements are universal and can be used for a wide variety of solutes, but with the limitation that a small variation in temperature will influence the refractive index of the solvent and disturb the measurement. The sensitivity is therefore only moderate. [12] Amounts in the order of micrograms are detectable. [14]

Ultraviolet absorption and fluorescence detector

The ultraviolet absorption detector is based on the absorption of ultraviolet radiation by solutes in the eluate. Many molecules absorb in this region of the spectrum, due to the presence of π-electrons or lone pairs in the molecule. In an ultraviolet absorption detector the eluate is irradiated with ultraviolet radiation, often 254 nm radiation from a mercury lamp[14], and the presence of a solute is detected by conventional absorption spectroscopy and using the Beer-Lambert law as described in Chapter 2. Both a single-wavelength or a multi-wavelength source can be used, and by focusing on a wavelength specific to a known analyte the technique can be made more selective. Since it is reasonably universal and simple, this technique is widely used.[12] Quantities in the order of nanograms are detectable.[14]

A variation of ultraviolet detection is fluorescence detection. In this technique the eluate is irradiated, and the fluorescence from the solute is detected. Since fluorescence upon irradiation at a chosen wavelength can be very specific for a given molecule, the technique can be made very selective by tuning the excitation and detection wavelengths. The lowest detectable quantities are in the order of picograms.[14]

Mass spectrometry detector

The coupling of mass spectrometry with chromatography is a truly successful one with numerous advantages over the detection methods described so far. A mass spectrum of the solute in the eluate is obtained, providing additional structural information about the solute.[15] Since mass spectrometry is a very sensitive method, another advantage is the small amount (of the order of picograms[15]) that can be detected. This method of detection is very powerful, but the requirement for a the mass spectrometer makes it a very expensive and complex detection method.

An overview of the detection limits of the various types of detector is shown in Table 3.1.

Table 3.1: Overview of the detection limits of the liquid chromatography detectors discussed in the text.

detector	lowest detectable quantity	reference
refractive index detector	µg	14
ultraviolet absorption detector	ng	14
fluorescence detector	pg	14
mass spectrometer	pg	15
evaporative light scattering detector	ng~µg	14

3.2.2 Evaporative light scattering detection

The ELSD is a relatively simple and inexpensive detector for liquid chromatography, which was described first by Ford and Kennard in 1966.[16] It makes use of the scattering properties of the solute. It works by evaporating the solvent, after which scattering by the solute is detected.[17] The

detection limit is in the order between nanograms and micrograms.[14]

Even though the ELSD has important advantages, such as its truly universal character and the fact that it is relatively inexpensive, its detection limit is high compared to other detection methods. Modifications that make the ELSD more sensitive are therefore well worth investigating and could contribute to the field of liquid chromatography by providing a universal, inexpensive and sensitive detector.

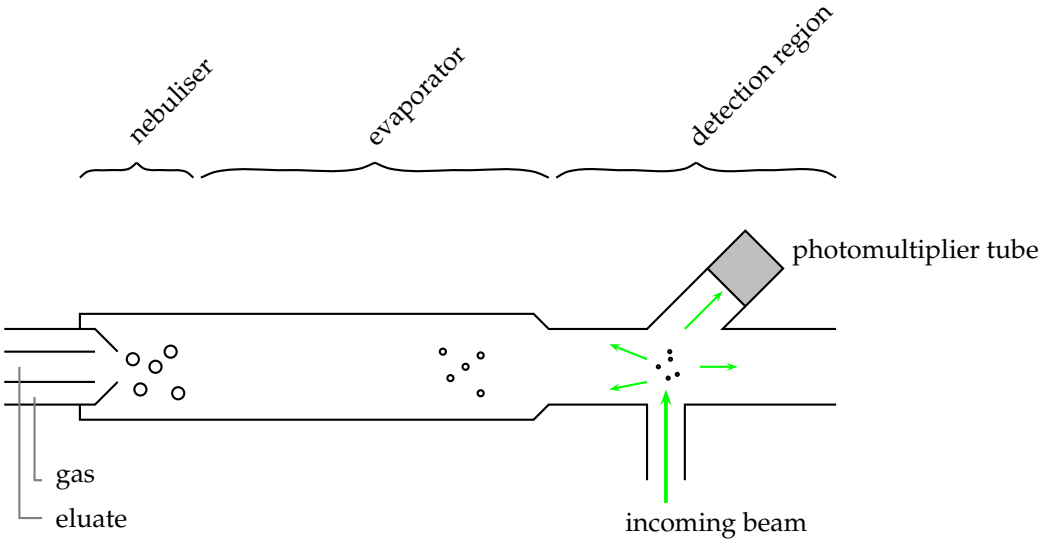

Figure 3.1: A schematic drawing of an ELSD. The eluate enters the nebuliser on the left side of the figure, where it becomes nebulised using a gas under pressure (for example N_2). The droplets travel with the gas flow through the evaporator, where the solvent is evaporated. In the detection region the solute is detected by measuring the intensity of scattered light from a light source, for example a tungsten lamp.

A schematic drawing of the operating principle of the ELSD is shown in Figure 3.1. The first step is nebulising the eluate into small droplets by mixing it with a gas stream at high temperature. This creates a large surface area, making evaporation of the solvent relatively fast. A variety of properties can be controlled, for example the flow rate of the eluate, the flow rate of the gas, and the temperature. Together with the properties of the eluate, such as surface tension, density and viscosity, this determines the size of the droplets. The droplet size after nebulisation is given by[18]

$$\delta_0 = \frac{585\sqrt{\gamma_1}}{2u\sqrt{\rho_1}} + \frac{597}{2}\left(\frac{\mu_1}{10\sqrt{\gamma_1\rho_1}}\right)^{0.45}\left(\frac{1000Q_1}{Q_g}\right)^{1.5}, \tag{3.2}$$

where δ_0 is the droplet radius in μm, γ_1 the surface tension of the solvent in $\mathrm{mN\,m^{-1}}$, u the difference in velocity between the nebuliser gas and the eluate in $\mathrm{m\,s^{-1}}$, ρ_1 the density of the solvent in $\mathrm{g\,mL^{-1}}$, μ_1 the eluate viscosity in Pa s, and $\frac{Q_1}{Q_g}$ the ratio between the eluate and nebuliser gas volumetric flow rates. This equation is purely empirical and was first proposed by Nuklyama

and Tanasawa in 1938.[19]

When the droplets pass through the nebuliser into the evaporator, where the applied temperature is higher, typically higher than the boiling point of the eluent, the solvent is evaporated. All solutes that are less volatile than the solvent will evaporate at a lower rate and the solute molecules from one droplet will form a cluster after the solvent is evaporated. The size of such a cluster can be calculated using

$$\delta = \delta_0 \left(\frac{c}{\rho}\right)^{\frac{1}{3}}, \tag{3.3}$$

in which δ_0 is the droplet radius, δ the cluster radius, c the concentration of the solute in the sample and ρ the density of the solute, both in $\mathrm{g\,mL^{-1}}$.

After evaporation and cluster formation, the particles are carried with the gas flow into the detection region. A light source, for example a tungsten lamp, illuminates the particle stream, and a detector, for example a photomultiplier tube, is placed at a scattering angle of *ca.* 45°. When there is no solute in the eluate, no particles pass the detector. The light source is not in line with the detector, so no light is detected. If there is a non-volatile solute, the particles move through the light beam and scatter the light in all directions. Some of the scattered light is detected by the photomultiplier tube, thus giving a signal.

This mechanism clarifies some of the advantages of ELSD. The most widely used detection technique for liquid chromatography is ultraviolet absorption detection. Whereas not all solutes absorb radiation in the ultraviolet range, all particles do scatter light. Evaporative light scattering is therefore more versatile than ultraviolet detection.

The second advantage is that in an ELSD the solvent is evaporated, so any possible interactions of the detection step with the solvent are eliminated. In ultraviolet detection some solvents cannot be used owing to their strong absorption of ultraviolet radiation. As long as the solvent is more volatile than the solute, the solvent does not have any influence on the ELSD measurements, so a good comparison between different samples in different solvents (sometimes the use of one solvent cannot be achieved) is possible with evaporative light scattering.

Also, ELSD is a background free technique; a signal is only seen in the presence of particles, in contrast to an absorption measurement where a comparison is made between the transmitted light in the presence and absence of a sample. Looking for a small difference between two large quantities is experimentally more difficult.

To be able to say more about the response of the detector, we need to consider the light scattering process in more detail.

3.2.3 Light scattering

When light interacts with a particle, or more generally an inhomogeneity in space, the light will be scattered by this particle or inhomogeneity. Depending on the size and shape of the particle, the effectiveness and direction of scattering may depend on a variety of factors. This is described

by different types of scattering:

- Rayleigh scattering, for particles which are much smaller than the wavelength of the incident light;
- Mie scattering, for particles with sizes comparable to the wavelength of light;
- geometric scattering, which emerges from refraction and reflection, for particles much larger than the wavelength.

Typical values for the expected particle size δ fall in the range from much smaller to the same order of magnitude of visible light[20], spanning the range between Rayleigh and Mie scattering.[21] Both are thus used when describing the scattering in an ELSD.

Rayleigh scattering

Rayleigh scattering was originally described by Strutt, Lord Rayleigh, in 1871.[22] His description is applicable to scattering from particles which have a negligible size compared to the wavelength of the scattered light.

One can consider the electric field ψ_0 of an incoming electromagnetic wave with angular frequency ω and amplitude A at some point, where a scattering particle is present, by

$$\psi_0 = A \, \exp\Big[- \mathrm{i}\, \omega t \Big]. \tag{3.4}$$

This electric field induces a dipole p in the scattering particle, which depends on the polarisability α of the particle

$$p = \alpha \, \psi_0 = \alpha \, A \, \exp\Big[- \mathrm{i}\, \omega t \Big]. \tag{3.5}$$

It was shown by Stokes in 1849[23] that for $k\delta \ll 1$ (k is the wave number, δ is the particle size) the electric field of radiation ψ_{sc} scattered from an oscillating dipole takes the form[24]

$$\psi_{\mathrm{sc}} = k^2 p \, \frac{\exp\Big[- \mathrm{i}\, (\omega t - kr) \Big] \sin\theta}{r}, \tag{3.6}$$

in which θ is the scattering angle (the angle between the incoming beam and the scattered beam) and r the distance from the scattering particle. The intensities are obtained by taking the absolute squares of the amplitudes, thus

$$I_0 = \psi_0 \psi_0^* = A^2; \tag{3.7}$$

$$I_{sc} = \psi_{sc}\psi_{sc}^{*} = k^4\alpha^2 A^2 \frac{\sin^2\theta}{r^2}. \tag{3.8}$$

The Lorentz-Lorenz equation expresses the polarisability α in terms of the refractive index n of the scattering particle. In the case of homogeneous spheres of radius δ this equation is[25]

$$\alpha = \left(\frac{n^2-1}{n^2+2}\right)\delta^3, \tag{3.9}$$

which results in

$$I_{sc} = k^4\delta^6 A^2 \frac{\sin^2\theta}{r^2}\left(\frac{n^2-1}{n^2+2}\right)^2. \tag{3.10}$$

For the conventional ELSD the intensity of the light scattered in the direction of the detector is the relevant measure for the detection signal. The detector is positioned at an angle of 45°, resulting in the scattered intensity

$$I_{sc} = \frac{k^4\delta^6 A^2}{2\,r^2}\left(\frac{n^2-1}{n^2+2}\right)^2. \tag{3.11}$$

A fundamental difference between the conventional scattering detection in the ELSD and detection via CRDS is that in the former, the scattered light is measured directly, while in the latter, the extent of attenuation of the light beam caused by scattering is measured. For the cavity ring-down measurements the total scattering cross section is relevant. The scattering cross section σ_s is given by[26]

$$\sigma_s = \frac{r^2}{I_0}\int I_{sc}\ \mathrm{d}\Omega = \int_0^{2\pi}\int_0^{\pi} I_{sc}\sin\theta\,\mathrm{d}\theta\,\mathrm{d}\phi, \tag{3.12}$$

in which Ω is the solid angle, $\mathrm{d}\Omega = \sin\theta\,\mathrm{d}\theta\,\mathrm{d}\phi$ (the coordinate system is chosen in such a way that the polar angle coincides with the scattering angle, thus both are referred to as θ) and the integral is over the whole sphere. Substituting Equation 3.11 into the equation above, and using the integral $\int_0^{\pi}\sin^3 x\ \mathrm{d}\,x = \frac{4}{3}$, the resulting scattering cross section is ‡

$$\sigma_s = \frac{8\pi k^4\delta^6}{3}\left(\frac{n^2-1}{n^2+2}\right)^2. \tag{3.13}$$

‡ Equation 3.13 also explains the blue colour of the sky: blue light, with a large wave number k, is scattered to a larger extent than the red light, with a small wave number. From the light of the sun mainly the blue light is scattered, resulting in the blue colour of the sky.

Mie scattering

For scattering from larger particles, with a size comparable to the wavelength of the incident light, the equations are not so straightforward. Solutions are obtained by solving Maxwell's equations for the interaction of light with a dielectric sphere. The equations are named after the physicist Gustav Mie, who first established these solutions in 1908.[27] Rayleigh scattering is a special case of these solutions, valid for particles very small compared to the wavelength. For larger particles, no simple expression for the scattering cross section as a function of the particle radius can be obtained, and the solution takes the form of a sum of an infinite series involving (spherical) Bessel functions.[24,28] A variety of readily available computer codes exist that can perform calculations using these series, and a MATLAB code from Mätzler[29] is used in the simulations below.

To show the behaviour of Mie scattering as a function of the particle radius, simulations for a chosen wavelength of light and refractive index were performed, while the particle size was varied. It is useful to plot this data as a function of $k\delta$, in which k is the wavenumber of the light and δ is the particle radius. In this way the particle size is easily seen in terms of the wavelength, which is the relevant comparison. For small particles $k\delta \ll 1$, which is the Rayleigh limit, and for particles with a size comparable to the wavelength of light $k\delta \approx 1$. For particles much larger than the wavelength of light $k\delta \gg 1$. The scattering intensity at a scattering angle of 45°, relevant for conventional ELSD, is plotted in Figure 3.2.

The scattering intensity in this graph behaves very differently from scattering in the Rayleigh

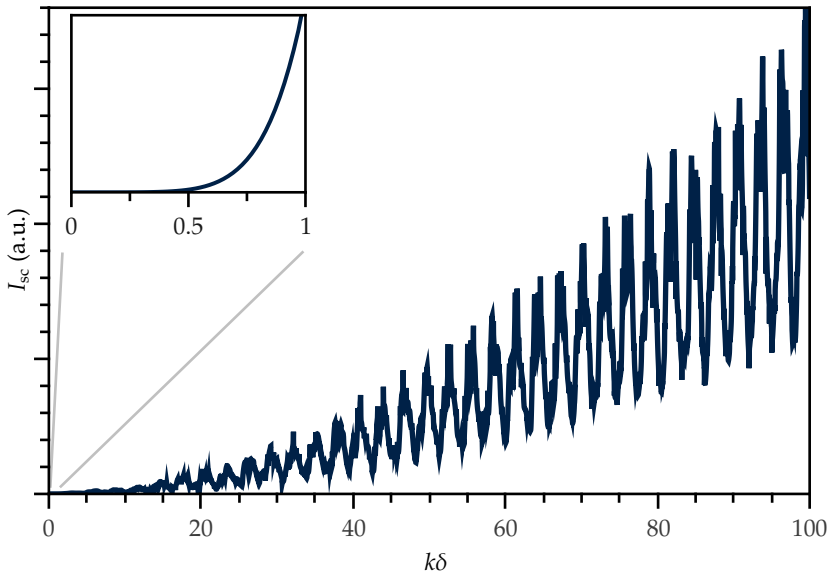

Figure 3.2: Simulation showing the scattered light intensity as a function of particle radius. The wavelength is 500 nm, the scattering angle 45° and the refractive index of the scattering particle has the real value of 1.5. The inset shows the Rayleigh range.

limit. While in the Rayleigh limit the scattered intensity depends simply on the sixth power of the

particle radius, in the range of Mie scattering there are minima and maxima due to interference effects. This distinct feature is often used in scattering experiments to determine the size of particles. This figure shows that there is no straightforward power relation between the scattered intensity and the particle radius. A similar relation is observed between the total scattering cross section and the particle radius, which is the relevant quantity for CRDS.

3.2.4 Detector response

Response in the Rayleigh limit

As explained in Section 3.2.2, the radius of the particles in the detection region of an ELSD is a function of the concentration. The relation between the concentration and radius is completely defined by Equation 3.3, assuming that the low concentrations of solute do not influence the viscosity, surface tension and density of the eluate and therefore do not influence δ_0. In the limit of Rayleigh scattering, the dependence of the scattered intensity on the concentration can be written, using Equations 3.3 and 3.11

$$I_{sc} = \frac{k^4 \delta^6 A^2}{2 r^2} \left(\frac{n^2 - 1}{n^2 + 2} \right)^2 = \frac{k^4 \delta_0^6 A^2}{2 r^2 \rho^2} \left(\frac{n^2 - 1}{n^2 + 2} \right)^2 c^2. \tag{3.14}$$

There is thus a quadratic relation between the intensity of the scattered light and the concentration of the sample for the conventional ELSD. Since the total scattering cross section shows the same dependence on δ as the scattered intensity at 45°, the cavity ring-down measurements depend in the same way on the concentration.

Response in Mie scattering regime

For Mie scattering there is not such a straightforward relation between scattered light and sample concentration. However, a closer look at the information available from Mie scattering calculations over the particle radius range of a few orders of magnitude can give an indication of the concentration dependence. When the logarithm of the scattered intensity at 45° is plotted as a function of the logarithm of the particle radius (or $k\delta$) and the resulting plot shows a straight line, the slope of this line reveals the power relation between these two quantities. Such a plot is shown in Figure 3.3.

For $k\delta \ll 1$, which represents the Rayleigh limit, the slope is 6. This corresponds to Equation 3.11, thus confirming that Rayleigh scattering is a special case of Mie scattering. For $k\delta \approx 1-10$ the dependence of the scattered intensity on the radius of the particle is less straightforward, while for larger radii a trend of slope two is approximated. For large spherical particles the scattering thus scales with the geometrical cross section, or δ^2, a result which is well known.[30] To fully treat the scattering by large particles, and particles with a large index of refraction, a geometric scattering approach is needed.

For the cavity ring-down measurements it is not the scattered intensity, but the scattering cross

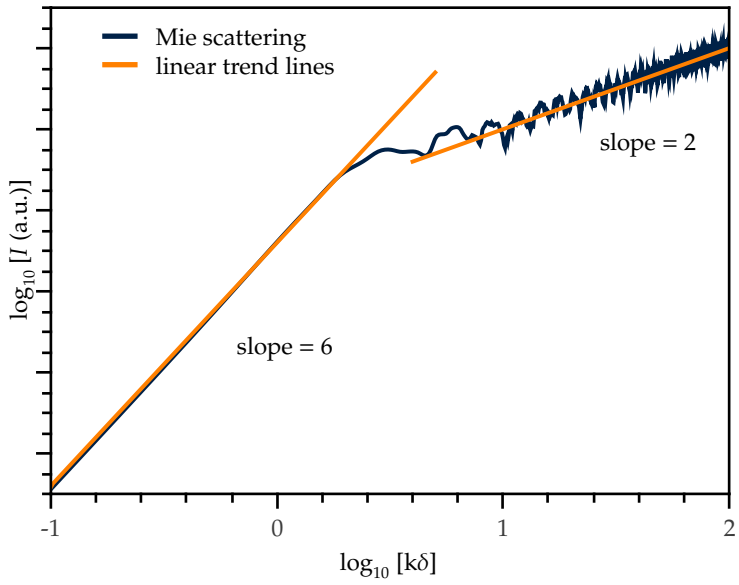

Figure 3.3: The scattered light intensity as a function of particle radius for a wavelength of 500 nm at a scattering angle of 45° for a particle with a real refractive index of 1.5.

section, that is relevant. The same method can be applied to the total scattering cross section for Mie scattering and the same dependencies on the particle size are observed

Concentration dependence

The radius δ of the particles scales with $c^{\frac{1}{3}}$. For the Rayleigh limit we see from Equation 3.13 that the cross section scales with δ^6 and therefore with c^2, as shown above. For larger spheres the cross section scales with δ^2 and therefore with $c^{\frac{2}{3}}$. For particles with $k\delta \approx 1 - 10$ there is nothing useful that can be concluded about the relation to the concentration. In this regime the scattering cross section can even decrease slightly with increasing concentration. To conclude, the relation between the concentration c and response S of the detector can be expressed as

$$S = h \cdot c^{f(c)}, \tag{3.15}$$

in which h and $f(c)$ are factors characteristic for the response. In this equation f is a function of the particle size and thus of the concentration: it is equal to 2 in the limit of Rayleigh scattering and $\frac{2}{3}$ in the limit of very large particles.

3.3 Experimental

The aim of the experiments is to verify whether CRDS can provide a more sensitive detection scheme for ELSD measurements. The ELSD is therefore central in the experimental setup. The operation principle of the detector was described in Section 3.2.2, and here the modifications made to a commercial ELSD instrument in order to accommodate detection by CRDS are described.

3.3.1 Modification of the evaporative light scattering detector

To enable a direct comparison to be made between the standard ELSD detection scheme and CRDS, a Polymer Laboratories PL-ELS 1000 donated to the project by Pfizer was modified to contain both an optical cavity and the conventional detection method. A schematic diagram of the cavity in the ELSD is shown in Figure 3.4.

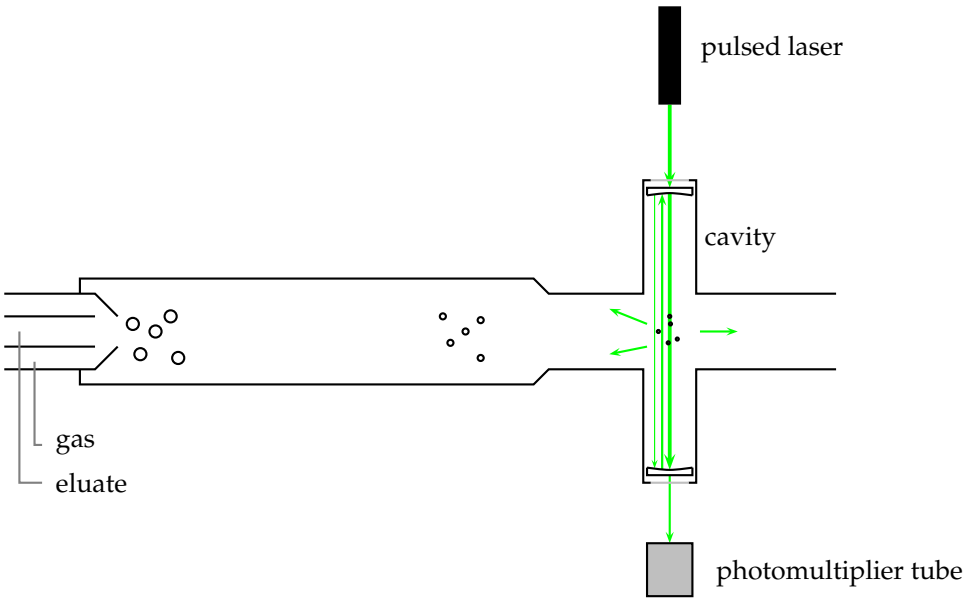

Figure 3.4: A schematic diagram of the modified ELSD. The conventional light source and photomultiplier tube (positioned orthogonally to the cavity and not included in the figure for purposes of clarity) are supplemented by a CRDS setup, to test the effectiveness of CRDS in this application.

The original ELSD detection setup, arranged orthogonally to the cavity in the modified instrument, is shown in Figure 3.1. The only modification to the instrument lies in the detection of the scattering, which is in this case performed using an optical cavity, a pulsed laser and a photomultiplier tube.

The cavity was created by attaching two hollow aluminium arms to the aluminium detection chamber, as shown in Figures 3.5 and 3.6. The arms contain the mirrors mounted on adjustable tilt stages to allow the cavity alignment to be optimised. The length of the cavity was 265 mm. Each arm was sealed with a glass window behind each mirror, to allow the detection chamber to be maintained at slightly higher than ambient pressure. The glass windows allow the laser

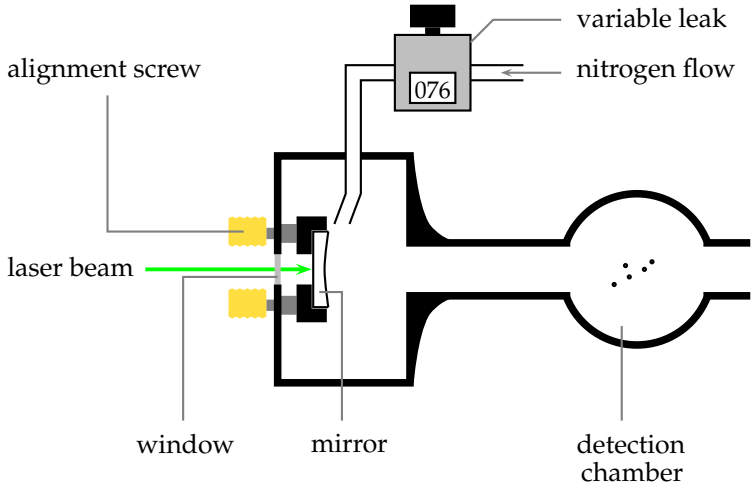

Figure 3.5: A schematic drawing of one half of the cavity, including the detection chamber. The other half of the cavity is constructed in the same way.

beam to enter the cavity on one side and to leave the cavity on the other side. The arms were black-anodised to minimise scattered light from the inside walls.

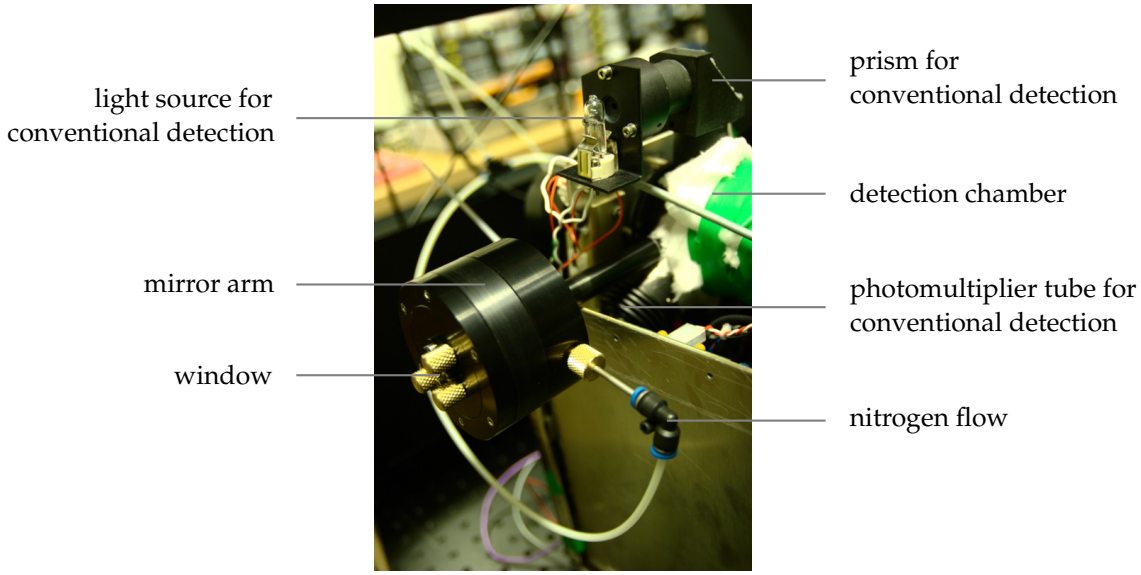

Figure 3.6: One of the mirror arms attached to the ELSD.

Overcoming various practical problems associated with the modifications constituted a major portion of the work involved in the project. For example, it took some time to establish a reliable method for mounting the arms to the chamber so that it could withstand the high temperatures reached during solvent evaporation, requiring the testing of a range of glues and cements. Welding was not possible due to the delicate internal construction of the ELSD.

The design of the cavity allows the intrusion of the particle cloud into the arms and also condensation onto the mirrors, which are colder than the gas flow. It was initially found that the

recovery of the ring-down time after sample injection was very long, undesirable for a chromatography detector. This was solved by flowing a low pressure of nitrogen into the arms close to each mirror. The flow was controlled by a Granville-Phillips series 203 variable leak valve, which was fed with 1 bar nitrogen and set at '00076'. This resulted in a pressure which was just sufficient to create a flow from the arms to the detection chamber, preventing particles from diffusing into the arms and depositing on the mirror surfaces.

For the conventional ELSD measurements the detector was connected to a Thurlby Thandar Instruments 1906 multimeter, to digitise the signal. The multimeter was coupled to a computer and the data was acquired with a LabVIEW programme written by Jason Lee. The ELSD makes use of a tungsten lamp as a light source and a photomultiplier tube to detect the scattered light. The detector was set at a nebuliser temperature of 90 °C and an evaporator temperature of 120 °C. Nitrogen flow gas was fed to the detector at a pressure of 5 bar, where it was regulated into a gas flow of 1.5 standard litres per minute.

3.3.2 Sample injection

Since the detector is normally used for liquid chromatography, mimicking the types of samples encountered in liquid chromatography was considered to be important. To simplify the experiment, the detector was not fed by a column, but was instead used to detect the injections of sample from a Rheodyne 7125 high-performance liquid chromatography (HPLC) six port injection valve with a 20 μL sample loop. Normally this valve is used to inject a sample into an HPLC column, and is correspondingly designed for a fast and precise injection. A schematic drawing of such a valve is shown in Figure 3.7.

The operation of the HPLC valve is started by setting it in the 'load' position. A Chemyx Fusion 400 syringe pump guarantees a 1.0 mL per minute continuous flow of eluent to the detector at any moment. In the 'load' position the sample can be injected into the sample loop, while any superfluous sample is fed out as waste. When the sample loop is filled, the valve can be turned to 'inject', in which position the eluent is fed through the sample loop, thus effectively injecting the sample into the ELSD. The valve can then be turned back to 'load' and the procedure can be repeated for a new injection.

3.3.3 Cavity ring-down spectroscopy

The experimental setup for the CRDS measurements is shown in Figure 3.8. The light source is a pulsed microchip Nd:YAG laser (Teem photonics SNP-08E-100, 8 μJ per 900 ps pulse, 7.4 kHz repetition rate) frequency doubled from 1 064 nm to 532 nm in an Ingcrys $KTiOPO_4$ non-linear crystal. The frequency-doubled beam is collimated by a 315 mm lens and reflected from a Thorlabs FM03 45° dichroic mirror in order to separate the fundamental and doubled beams. This infrared radiation is transmitted through the mirror and detected by a Thorlabs DET210 photodiode, which is used to trigger the oscilloscope to start measuring the ring-down event. The 532 mm beam is reflected and steered by a prism, through a second collimating lens, Thorlabs FGB37 335-610 nm

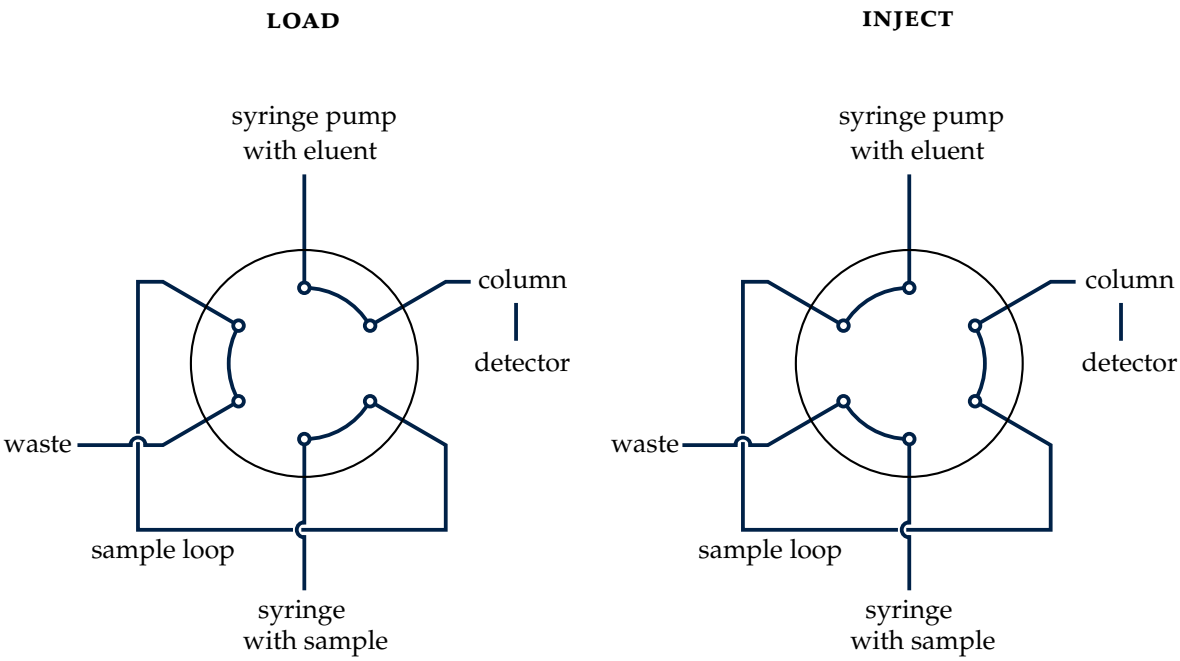

Figure 3.7: A schematic representation of an HPLC six port injection valve, used to inject the sample into the modified ELSD instrument. The valve has two modes. In one mode the syringe pump pumps the eluent directly into the column while the sample can be loaded in the sample loop ('load' mode). After turning the valve, the syringe pump pumps the eluent through the sample loop, effectively injecting the sample in the column ('inject' mode). A sample loop of 20 µL was used.

filter (to filter any remaining infrared radiation) and finally a 6 mm lens which couples the laser into a single mode optical fibre for delivery to the ELSD. To preserve the beam quality of the laser, a Thorlabs 460HP single mode optical fibre was used, with a core diameter of 8 microns.

The beam emerging from the fibre is collimated with a 6 mm lens, before entering the cavity. The 265 mm cavity is formed between a pair of Layertec highly reflective mirrors (R(0°,400-800 nm)=99.0±0.3 %, diameter=12.7 mm, curvature=500 mm). The light emerging from the cavity is detected with a Hamamatsu H10721-01 photomultiplier tube and monitored with a Tektronix TDS 2024B oscilloscope. The oscilloscope is coupled to a computer and the data acquired via a LabVIEW interface written by Jason Lee.[31] All of the components were mounted on an optical table and the optical elements were carefully cleaned before use.

3.3.4 Samples

Glucose solutions with concentrations ranging from 1 mg per litre to 20 g per litre were made using Milli-Q water and D-(+)-glucose (Sigma-Aldrich, ⩾99.5 %).

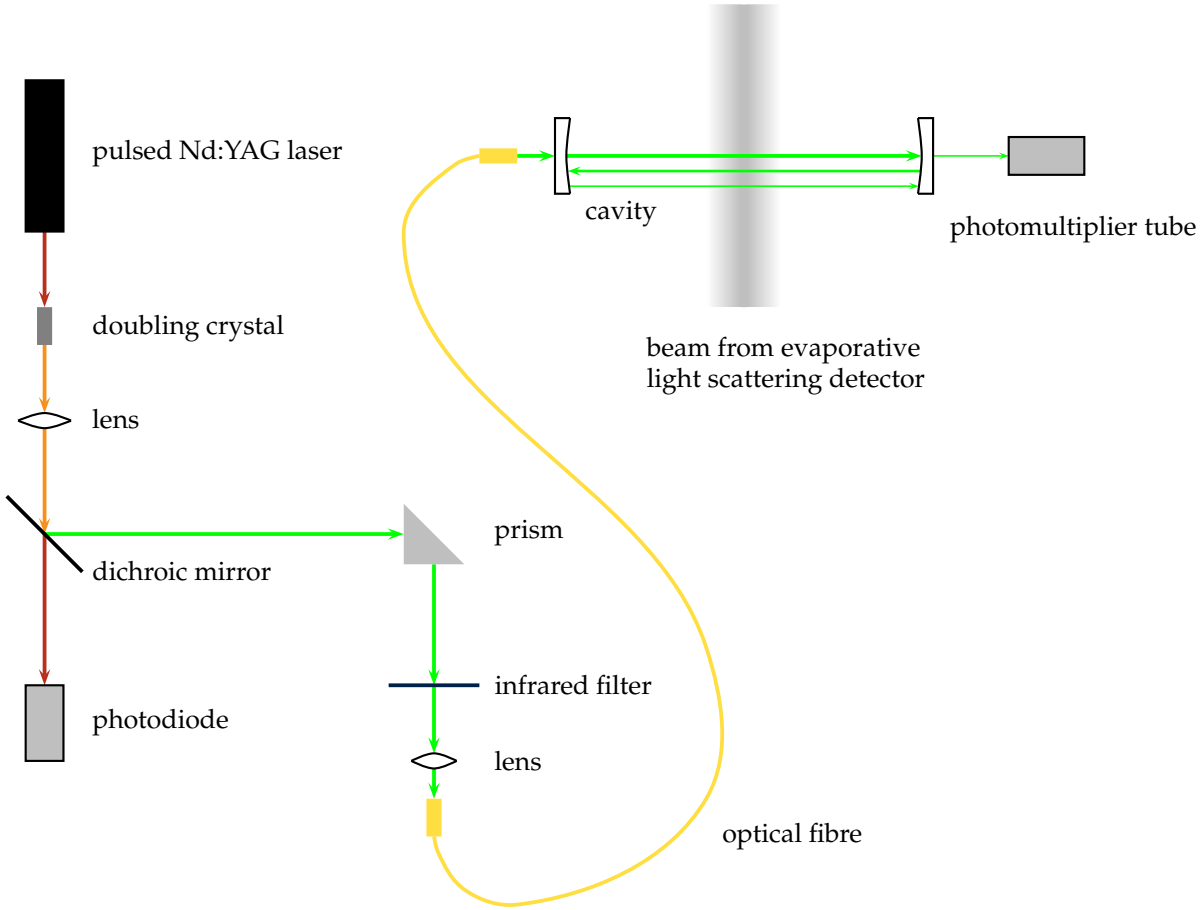

Figure 3.8: The experimental setup for CRDS. The Nd:YAG laser creates a pulsed beam with a wavelength of 1 064 nm and a pulse frequency of 7.4 kHz, which is frequency doubled to 532 nm by the $KTiOPO_4$ non-linear crystal. The first lens has a focal length of 315 mm, the lens focusing the beam into the single mode optical fibre used for beam delivery has a focal length of 6 mm. The cavity length is 265 mm and highly reflective mirrors with $R = 0.99$ are used. The photodiode monitoring the laser pulses is used to trigger the measurement with the photomultiplier tube.

3.4 Results and discussion

Before and after the ELSD was modified to use CRDS, the sensitivity of the detector was tested. The aim of the project is to investigate whether CRDS can improve the sensitivity of ELSD.

3.4.1 Conventional evaporative light scattering detection

Before modification

First the sensitivity of the apparatus in its original state was investigated. This was done by applying a water flow and using the HPLC six port valve to repeatedly inject glucose samples of a variety of concentrations from 1 mg per litre to 500 mg per litre. This is a reasonable approximation

of the sample conditions encountered in liquid chromatography. The results for a variety of concentrations are shown in Figure 3.9.

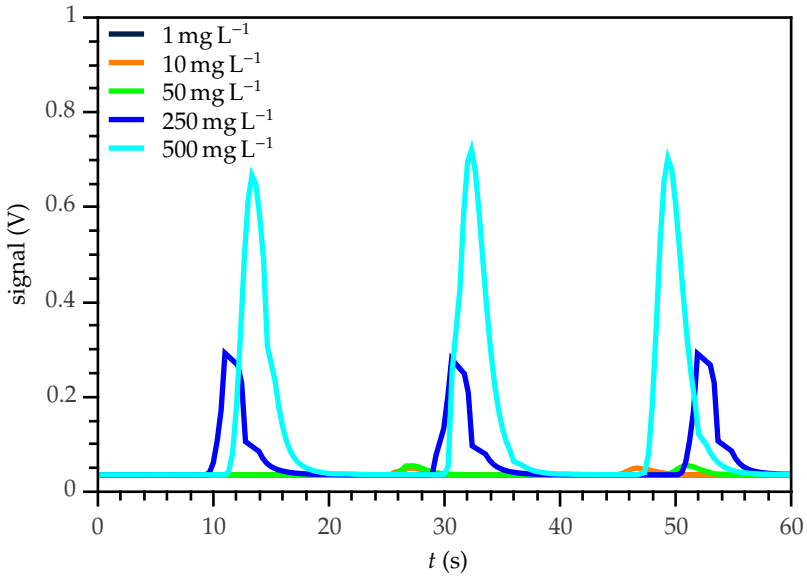

Figure 3.9: Measurements of injections with glucose solutions of a variety of concentrations before the modification of the ELSD.

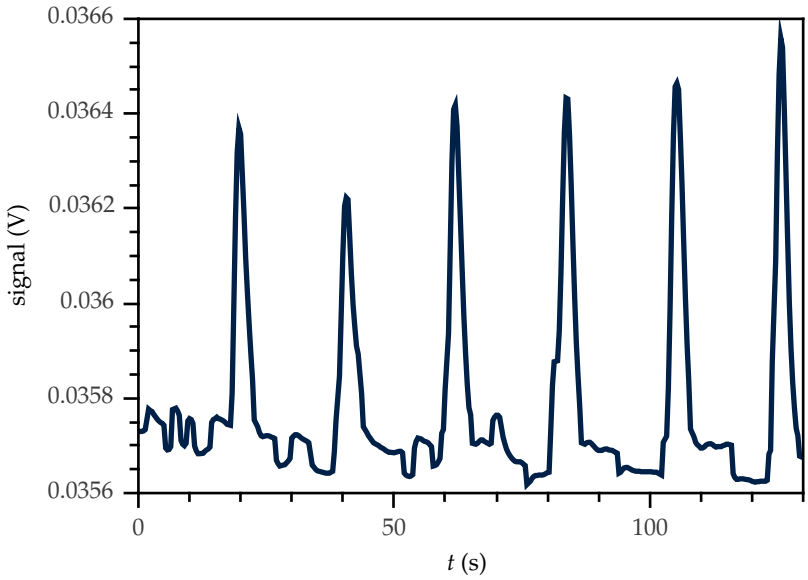

Figure 3.10: A closer look at the results for 1 mg L^{-1} from Figure 3.9.

The figure shows data from a number of glucose solution injections at concentrations ranging from 1 mg to 500 mg per litre. From this figure it is clear that a lower concentration results in a

lower measured signal, which is due to the smaller particle size. To determine the detection limit, a closer look is taken at the lowest measured concentration in Figure 3.10.

The lowest measurable signal is often defined as a signal that is three times larger than the noise in the baseline, so a signal-to-noise ratio of three. In the figure it is apparent that the noise has an amplitude of *ca.* 0.2 mV, while the signal is around 0.7 mV. It is clear that the injection of solutions with 1 mg L^{-1} glucose results in peaks that are above the detection limit. The detection limit of the ELSD before modification can thus be concluded to be below a concentration of 1 mg per litre. Lower concentrations were not measured before the modification, thus a more precise detection limit cannot be given.

After modification

For a number of reasons, the modification of the ELSD led to a reduction in the sensitivity of the conventional scattering measuring method. Two arms for the cavity mirrors were mounted to the detection chamber, through which a flow of nitrogen towards the detection chamber was applied. It is likely that this altered the flow properties in the detection chamber somewhat, therefore affecting the detected signal. Probably more importantly, in order to accommodate the arms containing the CRDS mirrors, it was necessary to remove one of the pair of lenses that focus scattered light from the interaction region into the photomultiplier tube. This was compensated for by replacing the remaining lens by a lens with a shorter focal length and optimising its position for maximum signal, but the focusing is no longer likely to be optimal, influencing the amount of light collected by the photomultiplier tube and therefore the sensitivity. To obtain the detection limit for conventional detection after modification, a second test with injections as described previously was carried out. The results are shown in Figure 3.11.

This figure should be compared to Figure 3.9 to confirm whether the detection limit has changed. From this comparison it becomes clear that the measured signal for comparable concentrations has decreased after the modification. Since all other experimental parameters are unchanged, this must be due to the modifications of the ELSD, most notably the change in optical elements in the detector. In Figure 3.12 a closer look is taken at the lowest measured concentrations.

From comparison of this figure with Figure 3.10 it is clear that the measured noise in the baseline has not changed and is still around 0.2 mV. The signal for 10 mg L^{-1} glucose sample is *ca.* 0.9 mV and for a 1 mg L^{-1} sample it is around 0.3 mV. This is lower than before modification, as observed for the higher concentrations too. For this reason the detection limit is higher. It can be seen that for a 10 mg L^{-1} glucose sample the signal is more than three times the noise, while for a 1 mg L^{-1} sample this is not the case. After modification the detection limit is thus between 1 and 10 mg L^{-1}, an increase of one order of magnitude.

Peak shape

The peaks in the chromatogram have a finite width, which is caused by the length of the injected pulse and diffusion while an injection is travelling through the tube feeding the detector. The intensity profile as a function of time emerges from molecular diffusion. A description of a sample

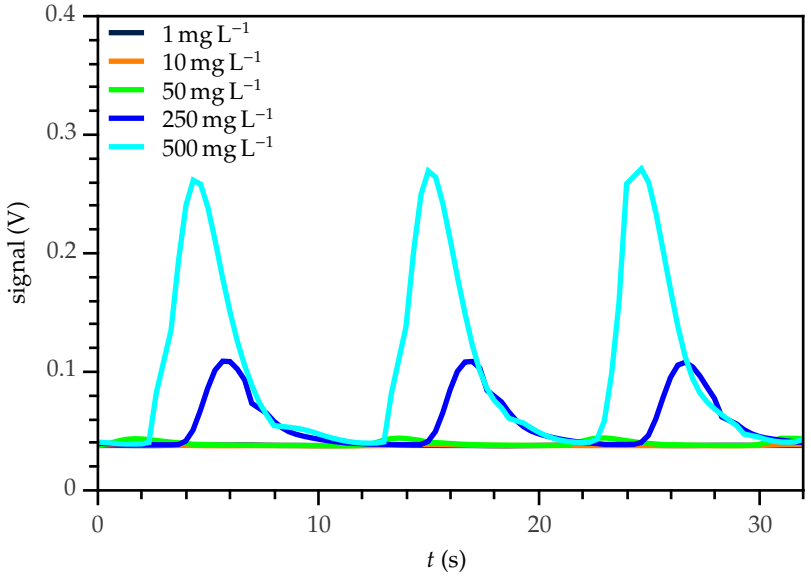

Figure 3.11: Measurements of injections with glucose solutions of a variety of concentrations after the modification of the ELSD. The data is recorded by conventional scattering detection.

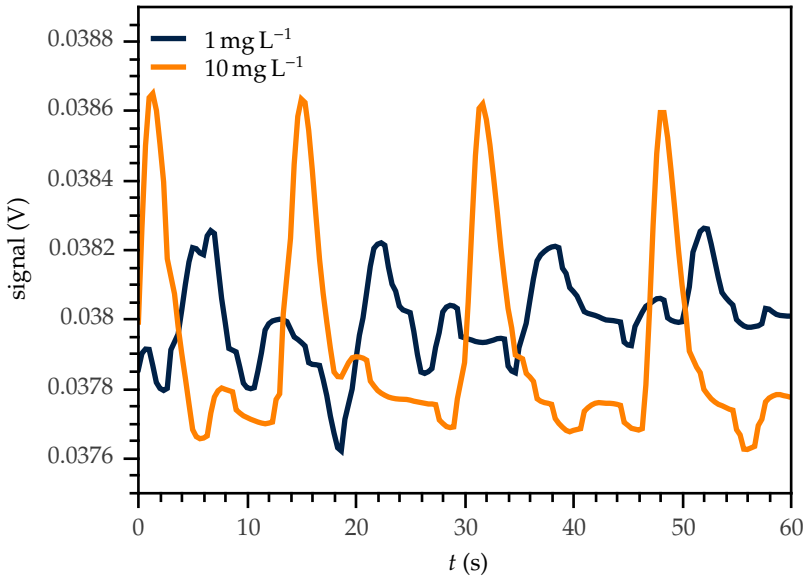

Figure 3.12: A closer look at the results for 1 and 10 mg L^{-1} glucose samples from Figure 3.11.

travelling through a linear tube is given by[32]

$$\bar{c}\,(t) = \frac{Vc}{2\pi R^2}\,\frac{1}{\sqrt{\pi k t}}\,\exp\left[\frac{-L^2\left(1-\frac{t}{\tau}\right)^2}{4kt}\right], \tag{3.16}$$

in which $\bar{c}\,(t)$ is the radially averaged intensity of the solute at time t, V is the volume of the injected sample, c the concentration of the injected sample, R the radius of the tube, k the dispersion coefficient, L the length of the tube and τ the average time it takes for a molecule to move through

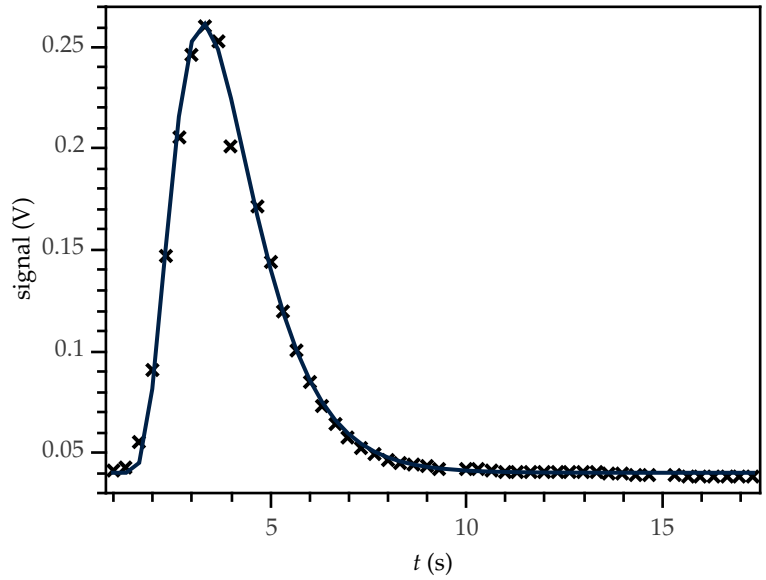

Figure 3.13: The fit of Equation 3.16 to the peak of injecting 20 µL of 500 mg per litre glucose solution. The points represent the measured data by conventional ELSD and the line is the fit of the equation to this data.

the tube. The fit of this equation to an example peak is shown in Figure 3.13. The peak was fitted using six parameters k_1 to k_6

$$S(t) = \frac{k_1}{\sqrt{k_2\,(t-k_3)}} \exp\left[\frac{-k_4\left(1-\frac{(t-k_3)}{k_5}\right)^2}{k_2\,(t-k_3)}\right] + k6, \tag{3.17}$$

in which $S(t)$ is the signal at time t. The fit to the data points is very good. Integration of the experimental peak data can create significant errors, since there are just a handful of data points for the peak, and instead a more reliable integration of the peak can be performed using the fitted curve instead, *i.e.* the peak area is given by the integral

$$A = \int_{k_3}^{\infty} \frac{k_1}{\sqrt{k_2\,(t-k_3)}} \exp\left[\frac{-k_4\left(1-\frac{(t-k_3)}{k_5}\right)^2}{k_2\,(t-k_3)}\right] \mathrm{d}t, \tag{3.18}$$

in which A is the peak area.

3.4.2 Cavity ring-down measurements

Ring-down signal

Example ring-down signals recorded for 532 nm laser pulses using the modified ELSD are shown in Figure 3.14. The blue line in this figure is a signal recorded for an empty cavity, while the orange

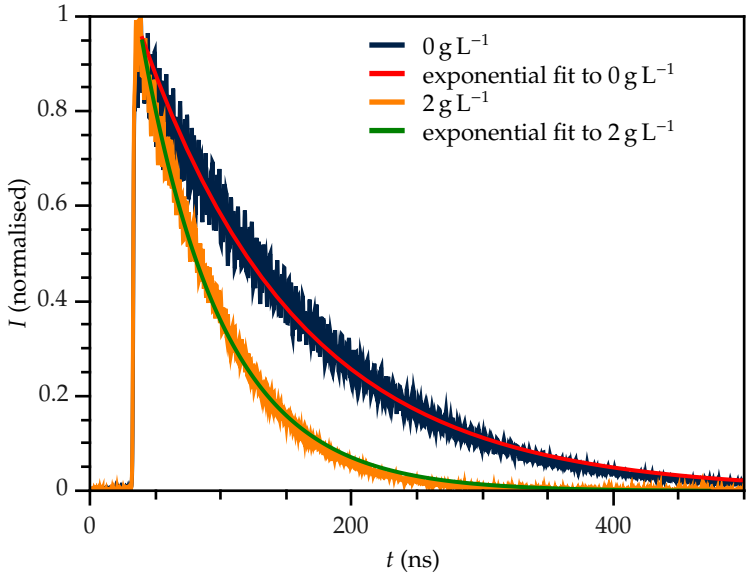

Figure 3.14: The signal after a laser pulse was sent into the optical cavity. For the blue line no absorbing or scattering particles were present in the cavity, for the orange line a continuous flow of 2 g L^{-1} glucose was applied. The red and green lines show single exponential fits to this data. It is visible that after injection of the glucose, the ring-down time has decreased from 122 ns to 62 ns. The signals are averaged over 16 laser shots.

line represents the signal recorded for a continuous flow of 2 mg L^{-1} glucose solution. The red and green lines are single exponential fits to the experimental data. In both situations an exponential decay was observed, as predicted by the 'photon bullet model' (see Chapter 2). The ring-down time in the empty cavity is 122 ns. According to Equation 2.10, the expected ring-down time in this cavity is 93 ns. The longer ring-down time indicates that the reflectivity of the mirrors at 532 nm was slightly higher than the 99 % stated by the manufacturer. At 532 nm, the ring-down time of 122 ns corresponds to a mirror reflectivity of 99.28 %, which is within the margin set by the manufacturer. When a flow of glucose solution is applied, the ring-down time decreases to 62 ns due to scattering in the ELSD.

Sensitivity

For cavity ring-down measurements, increased scattering causes a reduction in the decay time, as described earlier in Chapter 2. According to Equation 2.13, a chromatogram can be represented

by a plot of $\tau_0 - \tau$ as a function of time. A first test for a series of injections with a high glucose concentration is shown in Figure 3.15.

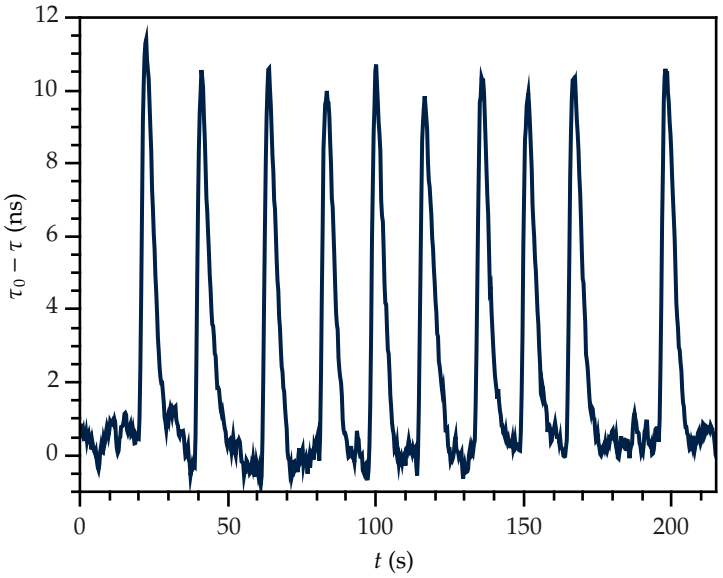

Figure 3.15: Measurements of injections of 20 µL glucose solution of 5 g per litre. The data is recorded with CRDS with mirrors that are 99 % reflective. Each point in the graph is an average of 16 laser shots.

The figure shows that the principle of applying CRDS to ELSD is viable. After injection, the ring-down time decreases. Noise is mainly caused by the accuracy with which one can determine the ring-down time from the ring-down data, which is typically ~1 % of the ring-down time. For the signals in this cavity, with a ring-down time of *ca.* 120 ns, this represents a noise level of roughly 1 ns. This is indeed the noise level observed in the chromatogram of Figure 3.15.

To further characterise the detection limit, measurements at lower concentrations were also conducted. The results are shown in Figure 3.16. In this figure the noise is still around 1 ns. It is clear that for 1 g L^{-1} glucose samples the signal is approximately equal to twice the noise, while a signal for 0.5 g L^{-1} is not observable. This means that the detection limit is approximately 1 g L^{-1}, about two orders of magnitude poorer than for conventional scattering detection after modification and about three orders of magnitude poorer than for conventional scattering detection before modification of the ELSD. The sensitivity of the cavity used in this experiment is modest and the effects of possible improvements are discussed in Section 3.4.3.

The detection limit of a cavity was described by Equation 2.15. Two factors can be modified to improve the detection limit. Firstly, the uncertainty in the decay time determination can be improved. This may not be very successful, since a noise level of 1 % was already achieved in this experiment. Secondly, the mirror reflectivity can be improved. Mirrors with a reflectivity of 99.99 % are among the best commercially available mirrors.

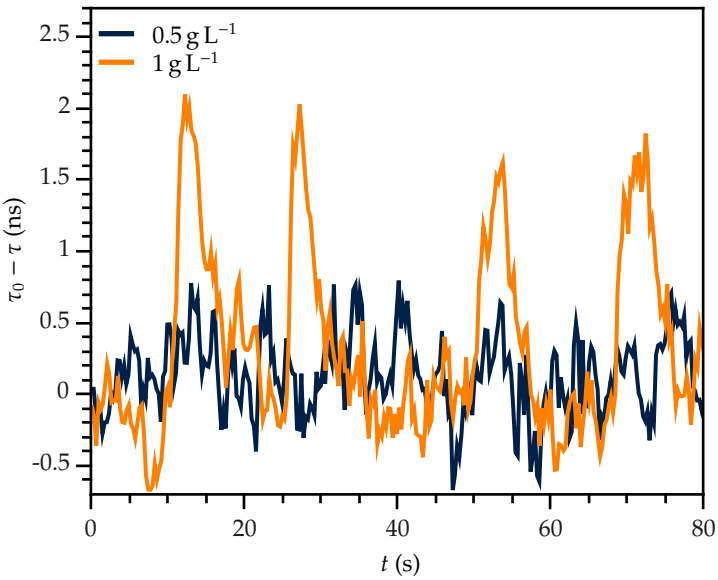

Figure 3.16: Measurements of injections with glucose solution of 1 and 10 mg L^{-1}. The data is recorded with CRDS with mirrors that are 99 % reflective. Each point in the graph is an average of 16 laser shots.

One attempt to improve the signal involved widening the beam into a collimated beam with a larger diameter in order to increase the interaction volume of the laser with the particle flow. The beam size before magnification was a few hundred microns. After modification the size was 3 mm, roughly half the diameter of the detection chamber. This did not improve the detected signal.

The laser beam was carefully aligned through the middle of the detection chamber to make the path length through the particle cloud as long as possible. While increasing the path length would undoubtedly improve the detection sensitivity, this cannot be achieved without drastic modifications to the design of the ELSD.

Averaging of more laser shots for each data point, a number of 64, 128 or 256 shots instead of 16, did not noticeably improve signal-to-noise ratio.

Peak shape

For the conventional scattering detection measurements resulting from the injection of a sample pulse, the peak shape could be related to diffusion. The shape of a single pulse recorded in the CRDS measurements is analysed in Figure 3.17. In this figure the intensity is represented by $\frac{\tau_0-\tau}{\tau_0\tau}$. In Equation 2.13 it was explained that this factor is proportional to the scattering cross section and number density of scattering particles, and this is therefore an appropriate quantity for comparison with the conventional measurements.

It is clear in this figure that the peak shape fits the distribution as described earlier. The

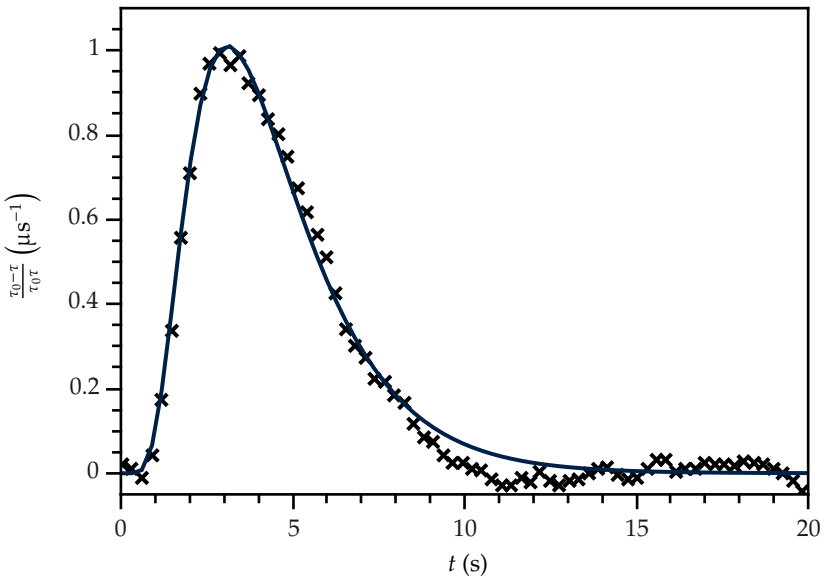

Figure 3.17: The fit of Equation 3.16 to the peak of injecting 20 µL of 5 g per litre glucose solution. The points represent the measured data by CRDS and the line is the fit of the equation to this data.

deviations from the fit are slightly larger than for the conventional scattering detection, which may be caused by uncertainties in the ring-down time determination. Since the peak shape is similar, it can be concluded that CRDS is suitable as a replacement for the conventional scattering detection, though not very useful due to the poor sensitivity.

3.4.3 Theoretical consideration of the detection limit

To explain the poorer sensitivity of CRDS that we have observed relative to the conventional ELSD, we can use Equation 2.15. For this experiment the mirrors have $R = 0.99$ and the diameter of the detection chamber is 5 mm, which provides a good approximation for the path length of the laser beam through the particle stream. The minimum error in the ring-down time determination is typically taken as three times the noise in the baseline. This error is 2 %, which results in $\kappa_{\text{min}} = 4 \cdot 10^{-4}\,\text{cm}^{-1}$.

This value for κ_{min} is four orders of magnitude higher than typically found in the CRDS literature[33,34], which is mainly due to the short path length of the laser beam through the sample and the relatively low reflectivity of the mirrors. In other experiments the path length of the laser beam through the sample is typically two orders of magnitude longer and the loss of the mirrors is typically two orders of magnitude lower. For this experimental setup this is therefore the best reachable κ_{min}.

To relate this κ to an injection concentration, the scattering in a sample of low concentration can be described by Rayleigh scattering, as in Equation 3.13. By dividing the eluate flow by the

particle volume, the number of particles n that is created in the nebuliser is found to be

$$n = \frac{Q_1}{\frac{4}{3}\pi\delta_0^3}, \tag{3.19}$$

in which Q_1 is the eluate flow rate. Then the number density of the particles N is obtained by dividing the number of particles by the flow rate of the gas Q_g

$$N = \frac{n}{Q_g} = \frac{3\,Q_1}{4\pi\,\delta_0^3\,Q_g}. \tag{3.20}$$

Combining these equations with Equation 3.3 and 2.15, the resulting equation for the detection limit is

$$c_{\min} = \rho\sqrt{\frac{\kappa_{\min}}{2\,k^4\,\delta_0^3}\frac{Q_g}{Q_1}\left(\frac{n^2+2}{n^2-1}\right)^2}. \tag{3.21}$$

To obtain a typical value, green light (using $k = \frac{2\pi}{\lambda}$ with λ =532 nm) is assumed. For glucose[35] ρ =1.562 g mL^{-1}, the refractive index is estimated to be 1.5, the eluate flow rate is 1 mL min^{-1} and the gas flow is 1.5 L min^{-1}. The quantity which is hardest to estimate is δ_0. In literature it is found that this is typically in the order of 5 µm.[20]

This results in $c_{\min}$ = 19 mg L^{-1}. This is higher than the detection limit of the ELSD in its original state. Additionally, this is a theoretical value only. In a real experiment many factors will inherently increase the detection limit. The ELSD filters out part of the droplets, to create a more uniform particle size distribution. In this way a significant fraction of the particles is lost. Also, the concentration of the injected sample is not equal to the concentration in the detector, since diffusion in the feeding tube decreases this concentration dramatically. Particles can also be lost during the nebulisation or evaporation. These and other reasons will cause the experimentally determined detection limit to be much higher. This supports that our current CRDS setup is not sensitive enough to enhance the sensitivity of the ELSD.

Improvements are possible by using mirrors with a lower loss and by bringing down the error in the ring-down time determination. The best available mirrors have reflectivities of R = 0.9999. The error in ring-down time can be brought down by taking into account any background signal of the photomultiplier tube, minimising the deviations from a single exponential decay in the ring-down trace. An error (three times the noise) of 0.7 % can be achieved in our lab.[36] Bechtel *et al.* have achieved an error of 0.05 % with a continuous wave laser.[37] With an improvement of bringing it down from 2 % to 0.02 %, which is very optimistic for what is experimentally possible, and better mirrors the theoretical limit is brought down by a factor of 32 to ~0.6 mg L^{-1}. If these improvements bring down the measured detection limit to the same extent, the detection limit will be approximately 30 mg L^{-1}. This is still about two orders of magnitude worse than the ELSD

before modification, but only five times worse than performance after modification.

From an experimental point of view this can be explained by the approaches of both techniques. In the conventional ELSD detector there is no signal in the absence of scattering particles. A low concentration gives a few scattered photons. Low light intensities against an absent background can easily be detected with a photomultiplier tube. For the CRDS experiment the scattering causes a small change in a large quantity, the ring-down time. Observing very small changes in this quantity with its fluctuations is experimentally more difficult.

Since it is not precisely known what caused the decrease in sensitivity after modification for the conventional measuring method, we conclude that with an optimised CRDS setup a sensitivity close to the conventional measurement method might be achieved. By designing an ELSD specifically for CRDS, in which the path length is longer, a sensitivity comparable to the conventional method or even better may be achieved.

Chapter 4

Headspace absorption spectroscopy

4.1 Introduction

Cavity ring-down spectroscopy is widely used nowadays in the field of analytical chemistry. While CRDS was originally developed for gas-phase analysis, which remains the largest field of application, over the last decade there have been numerous examples in which CRDS has been applied to the analysis of liquid-phase samples.[38] Liquid-phase analysis in a cavity is much more challenging than gas-phase analysis, primarily because the sensitivity is often limited by containment of the liquid sample in an absorption cell inside the cavity. The reflection and scattering losses at the interfaces, as well as attenuation via absorption in the cell walls, will typically dominate over the mirror losses. This is in contrast to gas-phase applications, for which the mirror losses dominate. While liquids can be placed in direct contact with the cavity mirrors, this is usually not a desirable solution, as the mirror reflectivity will drop[39] and the mirror surfaces can be damaged by the liquid.

A possibility which is explored in this chapter is probing a solution by performing CEAS measurements on the vapour phase above the solution, known as the headspace. Headspace analysis is an established sample preparation method in gas chromatography. A solution is equilibrated with its vapour phase, after which the vapours are injected in a gas chromatograph. Instead of gas chromatography, we propose that CRDS or CEAS can be used. A schematic representation of this idea is shown in Figure 4.1.

This method can find its way into many applications, one of which is following the kinetics of a reaction in solution. In this chapter the possibility of this is explored. Real-time gas-phase analysis using CRDS has already been applied to a variety of volatile chemical species, for example in breath analysis.[40,41,42] For this reason the method is promising for probing volatile molecules in solution.

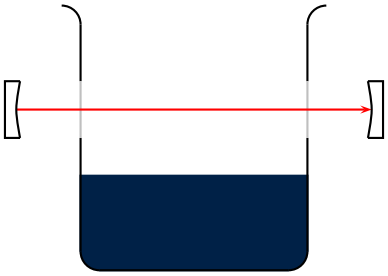

Figure 4.1: A schematic representation of headspace absorption spectroscopy. An optical cavity is used to probe the vapour phase above a solution.

4.2 Theory

The vapour pressure of a substance is defined as the pressure of its vapour when the vapour phase is in equilibrium with the condensed phase. This determines the number of molecules in the gas phase and is therefore a relevant quantity for headspace absorption spectroscopy. The vapour pressure of a component above an ideal solution is described by Raoult's law[43]

$$p_i = p_i^* x_i, \tag{4.1}$$

in which p_i is the vapour pressure of substance i in the solution, p_i^* is the vapour pressure of the pure substance and x_i is the mole fraction of the substance in the liquid phase. The law assumes ideal behaviour in the liquid phase, *i.e.* all interactions between molecules in the solution are identical, regardless of their identity. Most solutions do not display ideal behaviour, and reliable quantitative results can therefore not be expected when using Raoult's law. However, it can be used to indicate the order of magnitude for the number of particles in the vapour phase. The law can be used to calculate the number density of solute particles in the gas phase when it is combined with the ideal gas law[43]

$$pV = nk_BT, \tag{4.2}$$

in which V is the volume of the gas, n the number of particles, k_B the Boltzmann constant and T the temperature. The number density N can then be written as

$$N_i = \frac{n_i}{V} = \frac{p_i}{k_BT} = \frac{p_i^* x_i}{k_BT}. \tag{4.3}$$

From this equation and Equation 2.15 it is clear that the detection sensitivity depends both on the volatility and the absorption cross section of the molecule of interest. Taking into account the experimental possibilities, a set of three dyes was chosen to be studied. At first the technique was applied to guaiazulene, whose structure is shown in Figure 4.2. Due to its low molecular weight, it is expected that this dye will evaporate sufficiently. This dye could be probed with a 635 nm diode laser.

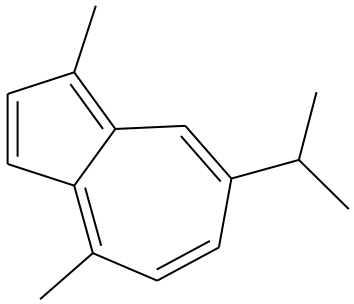

Figure 4.2: The structural formula of guaiazulene.

Solutions of potassium permanganate and sulforhodamine 101 were also investigated, due to their high absorption coefficient at 532 nm, the wavelength of our frequency doubled Nd:YAG laser.

4.3 Experimental

4.3.1 Samples

The first experiments were conducted using solutions of 0.55 g and 20 g per litre guaiazulene (Sigma-Aldrich, 99 %) in ethanol (Sigma-Aldrich, ⩾99.8 %). Guaiazulene is a relatively volatile dye with a strong absorption in the visible part of the spectrum due to a conjugated π-electron system. Two other dye solutions that were prepared are potassium permanganate ($KMnO_4$, Alfa Aeser, 99 %) at a concentration of 0.011 g and 20 g per litre in Milli-Q water and sulforhodamine 101 (Lambda Physik) in Milli-Q water at 0.002 g and 1 g per litre.

Absorption spectra were recorded for all the dyes using a Thermo Scientific Evolution 220 UV-Visible spectrophotometer with a 1 cm cuvette to confirm that the chosen dyes showed significant absorption at the wavelengths of the probing lasers.

4.3.2 Cavity enhanced absorption spectroscopy

Optical setup for 635 nm absorption measurements

For the first headspace absorption spectroscopy experiment a red diode laser (Power Technolgy PPMT03(635-5B)G3, 3.0 mW) was used. Since the continuous output power of this laser is only 3 mW, it was not suitable for pulsed CRDS experiments. Pulsing the laser with very short pulse durations would reduce the output power to such a large extent, that not enough light would be

coupled into the cavity to detect the output from the cavity. A CEAS experiment, see Section 2.3, was set up instead, shown in Figure 4.3.

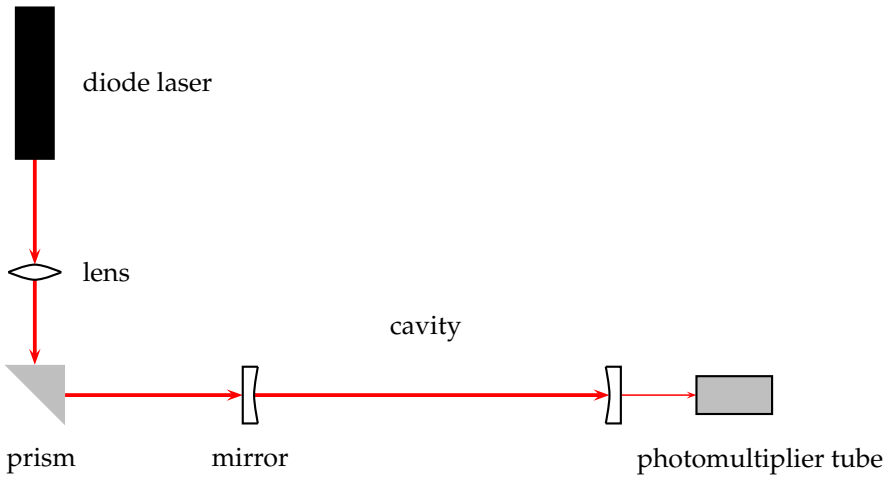

Figure 4.3: The CEAS setup used in this experiment. A red diode laser with a wavelength of 635 nm is focused by a 500 mm lens. The beam is then directed through a prism to facilitate alignment of the beam through the cavity. Mirrors with $R = 0.99$ are used and the cavity length is 585 mm.

The continuous wave 635 nm diode laser beam is directed through a lens with a focal length of 500 mm to focus the beam into the cavity. A prism is used to steer the beam into the cavity, which is formed from a pair of Layertec highly reflective mirrors (R(0°,400-800 nm)=99.0±0.3 %, diameter=12.7 mm, curvature=500 mm). The length of the cavity is 585 mm. The signal is detected with a Hamamatsu H10721-01 photomultiplier tube and monitored with a Thurlby Thandar Instruments 1906 multimeter. The multimeter was interfaced to a computer and the data was acquired with a LabVIEW programme written by Jason Lee. All of the equipment was mounted on an optical table and the optical elements were carefully cleaned before use.

Optical setup for 532 nm absorption measurements

The optical setup for the 532 nm absorption measurements was essentially the same as the setup used for the ELSD experiment, as shown in Figure 3.8. The only differences were the cavity length, which was 585 mm for the headspace experiment, and the mirrors that were used, CVI Melles Griot highly reflective mirrors (R(532 nm)=99.8 %, diameter=25 mm, curvature=1 000 mm).

4.3.3 Sample arrangements

Open air setup

First an 'open air' experiment was done, in which the laser beam sampled the vapour phase above a Petri dish with a diameter of 120 mm. The distance between the laser beam and liquid surface

was 5 mm. To limit the influence of air flows in the laboratory, a 'chimney' constructed from cardboard was placed around the Petri dish, as shown in Figure 4.4.

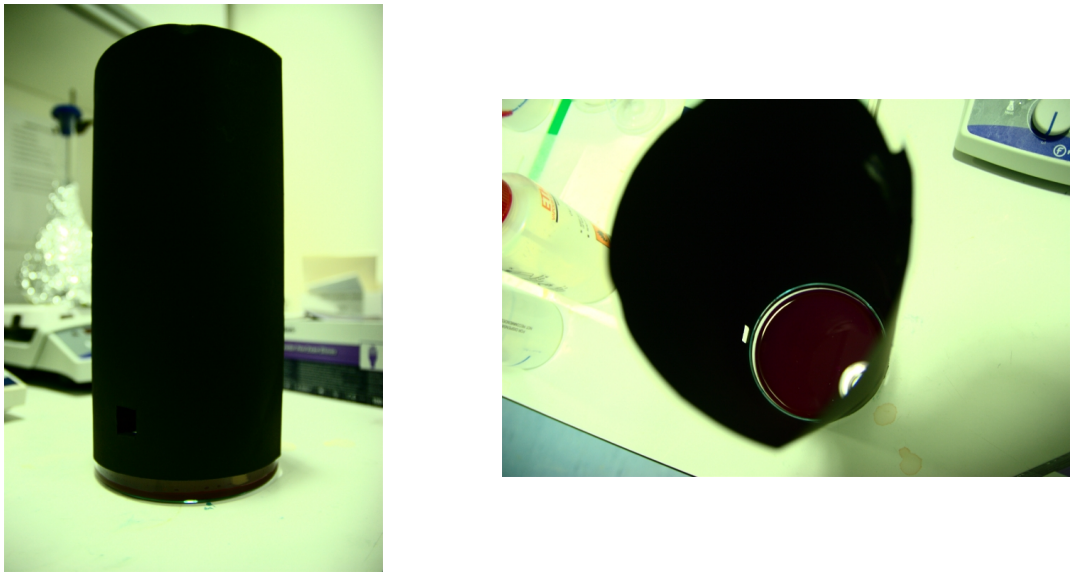

(a) (b)

Figure 4.4: The Petri dish with a cardboard chimney attached to it, as used in the open air experiment.

For the room-temperature measurements the CEAS signal was recorded continuously, firstly for an empty Petri dish and then after the Petri dish had been filled to the desired level, with the sample of interest.

Measurements at a higher temperature were conducted by placing the Petri dish on a hot plate. The solution of interest was warmed up to the desired temperature and a waiting time of half an hour was taken to let the vapour phase equilibrate. The CEAS signal was recorded for this solution at high temperature, after which the Petri dish was moved out of the cavity to measure the CEAS signal in the absence of the vapour.

Vacuum chamber setup

For conducting more controlled experiments, a vacuum chamber setup was built. This is a closed system which allows a low pressure to be maintained which can be measured and controlled. The liquid sample is allowed to reach equilibrium with its vapour inside the vacuum chamber, after which the measurement can be taken. In this way fluctuations due to evaporation of the mixture are minimised and the low pressure enhances the evaporation of the mixture. The setup is shown schematically in Figure 4.5.

The optical cavity is housed within the stainless steel vacuum chamber, which is pumped by an Edwards 5 Two Stage vacuum pump. A Pfeiffer TPR 280 vacuum gauge, controlled by a Pfeiffer TPG 261 read-out unit, was connected to monitor the chamber pressure below one millibar. An analogue absolute vacuum gauge of S.M. Gauge company was added to measure higher pressures, above one millibar. A venting valve was connected to vent the vacuum chamber

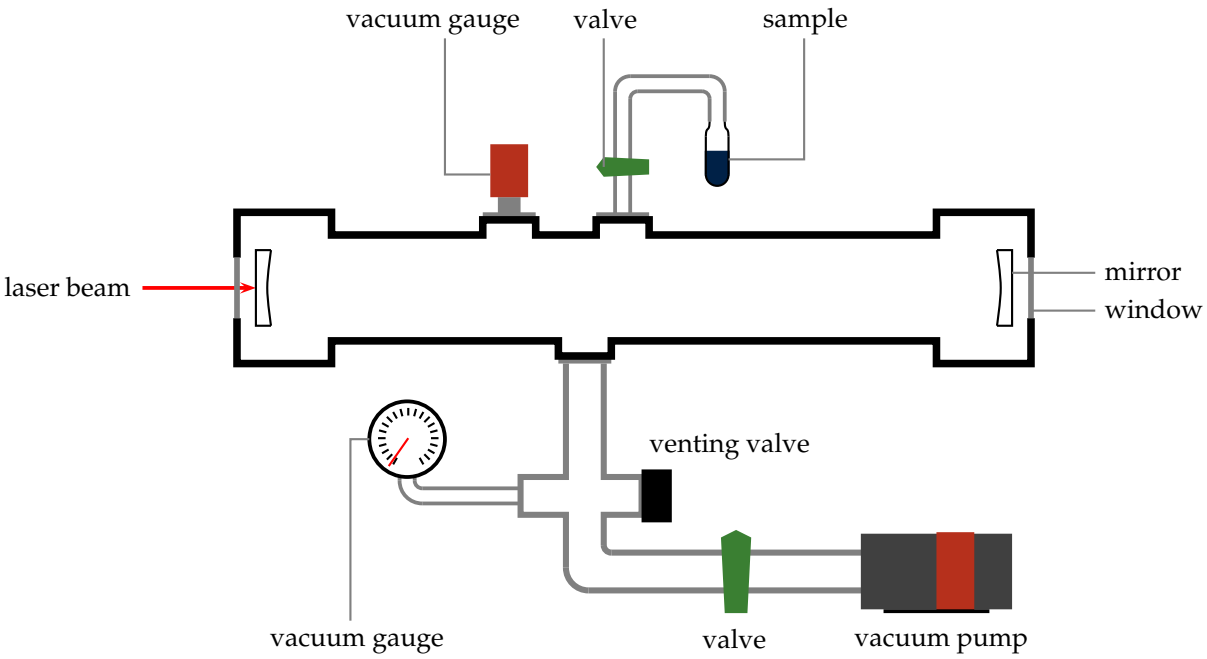

(a)

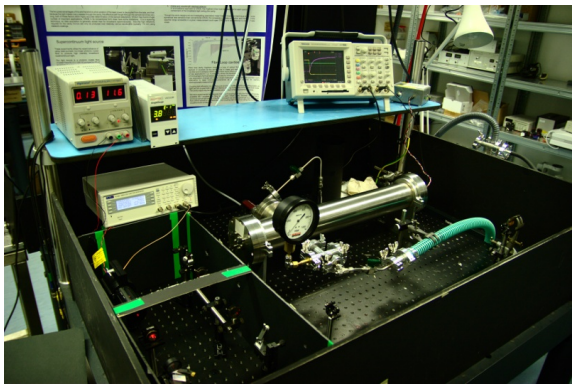

(b)

Figure 4.5: The experimental setup for headspace absorption spectroscopy. In the schematic drawing of Figure **(a)** the aluminium chamber is central, to which two vacuum gauges, a sample ampoule and the vacuum pump are attached. The laser beam is coupled in the cavity through a window and is allowed to leave the chamber through a window on the back side. In Figure **(b)** a photo of the experimental setup is shown.

back to atmospheric pressure after each experiment. A valve between the vacuum chamber and the vacuum pump allowed the chamber to be isolated from the pump during the experiment. The sample holder consisted of a glass ampoule sealed to a piece of stainless steel tubing and connected to the vacuum chamber via a Swagelok ball valve. The laser beam enters and leaves the chamber through fused silica windows. The setup was thoroughly checked for leaks using a helium mass spectrometer. A brief test of the vacuum system established the baseline pressure to be 0.07 mbar. After closing the chamber and turning off the vacuum pump, this pressure would rise slowly. In the absence of a sample, the pressure after 24 hours was approximately 1 mbar. Both this pressure and the baseline pressure are higher than the vapour pressure of a typical dye, but significantly lower than the vapour pressure of ethanol, which is at room temperature 78.7 mbar.[35]

An experiment was performed by first maintaining a low pressure in the chamber. The chamber was isolated from the vacuum pump and the valve to the sample was slowly opened. Since air was present in the sample holder, this valve was quickly closed again, the chamber brought back to low pressure, after which the chamber was isolated again. The chamber was then ready for the experiment, which was started by slowly opening the valve to the sample holder. During this the CEAS signal was recorded to observe any possible changes due to the evaporation of the dye.

4.4 Results and discussion

4.4.1 Absorption spectra

First the absorption spectrum of the guaiazulene was recorded with a conventional spectrophotometer. Figure 4.6 shows the measured absorption spectrum of a solution of 2.77 mM guaiazulene in ethanol. The orange line in the spectrum shows the wavelength of the laser used in the CEAS measurements. It is clear that the laser wavelength is close to the maximum of the absorption peak. At 635 nm the absorbance is 1.10, which corresponds to a molar extinction coefficient of 397 $\mathrm{L\,mol^{-1}\,cm^{-1}}$. The extinction coefficient ε is related to the absorption cross section $\sigma_a(\nu)$ by[44]

$$\sigma_a(\nu) = \frac{\varepsilon \ln 10}{10 N_A}, \tag{4.4}$$

in which N_A is the Avogadro constant. The absorption cross section at 635 nm is $1.52 \cdot 10^{-22}\ \mathrm{m^2}$.

For sulforhodamine 101 and $KMnO_4$ the absorption spectra are shown in Figure 4.7. For $KMnO_4$ the absorption of the laser light at 532 nm is very strong, in the middle of the absorption band, while this is not the case for sulforhodamine 101. Due to the high absorption cross section in the peak of sulforhodamine 101, the absorption even in the tail of the absorption band at 532 nm is nevertheless large. At 532 nm the absorption cross section for $KMnO_4$ is $5.71 \cdot 10^{-21}\ \mathrm{m^2}$ and for sulforhodamine 101 it is $1.35 \cdot 10^{-20}\ \mathrm{m^2}$.

It should be noted for all these dyes that the gas-phase spectrum, which is relevant for headspace absorption spectroscopy, is very likely to be different from the liquid-phase spec-

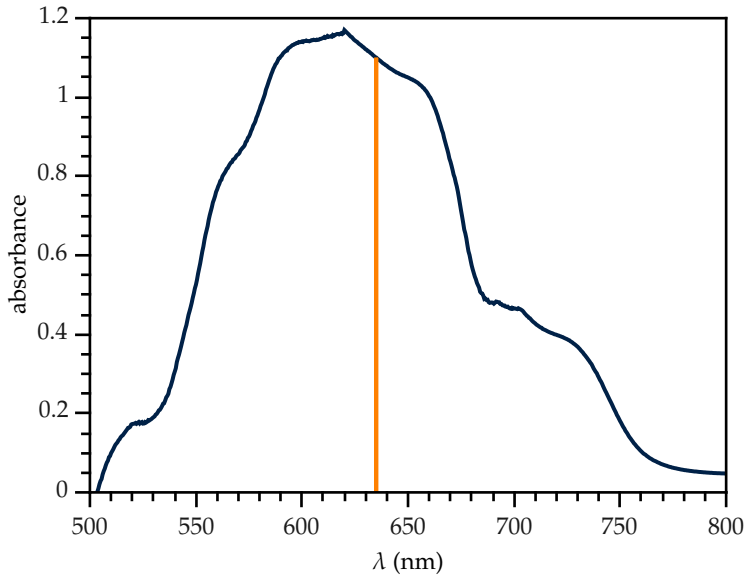

Figure 4.6: The absorption spectrum of a solution of 0.55 g L^{-1} (2.77 mM) guaiazulene in ethanol. The orange line denotes the laser wavelength, $\lambda = 635$ nm, used in the CEAS experiment and it is clear that this is close to the maximum of absorption.

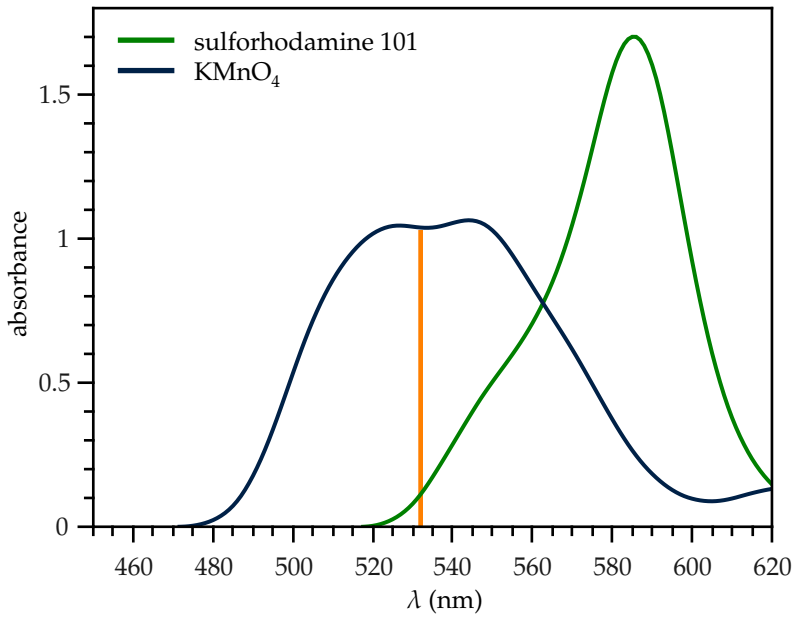

Figure 4.7: The absorption spectra of a solution of 0.011 g L^{-1} $KMnO_4$ in water and a solution of 0.002 g L^{-1} sulforhodamine 101 in water. The orange line denotes the laser wavelength, $\lambda = 532$ nm. This is for $KMnO_4$ in the middle of the absorption band, for sulforhodamine it is not in the maximum.

trum. Vibrational and rotational structures may be resolved in the gas phase, but measuring this spectrum is very difficult. In literature no gas-phase spectra could be found for these dyes, so it has to be kept in mind that the lasers may be probing at wavelengths that are not in the middle of a peak in the gas phase.

4.4.2 Open air experiment

Before making measurements on the solutes of interest, the intensity from the back mirror of the cavity was monitored in the open air setup upon adding ethanol to the Petri dish. In this way the sensitivity of the experiment to the presence of a non-absorbing, volatile solvent could be investigated. The result of this measurement is shown in Figure 4.8. The time period from 0

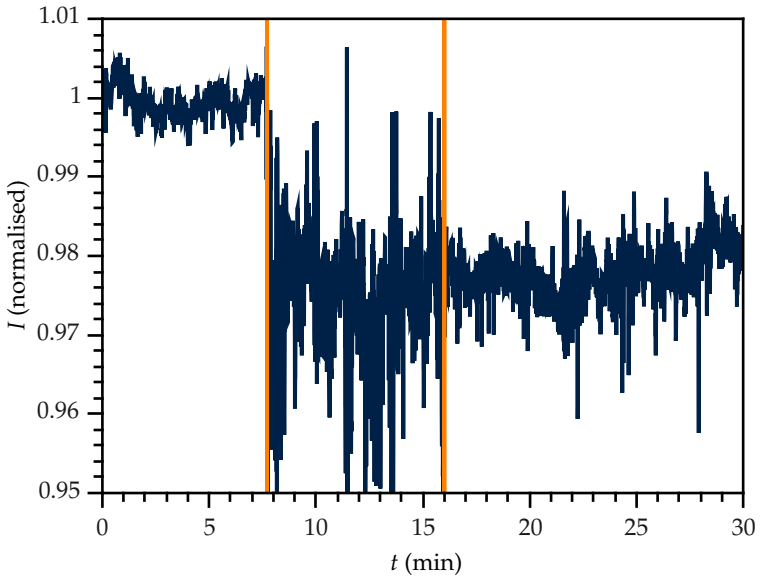

Figure 4.8: The CEAS signal recorded during the open air experiment on scattering from ethanol vapour. At times to the left of the first orange line the Petri dish was empty, after the first orange line ethanol was poured into the Petri dish. After the second orange line a lid was placed on the chimney.

to 8 minutes shows the intensity while the Petri dish is empty. There are some fluctuations in this intensity, which correlate with fluctuations in the laser output. This was confirmed by direct measurements of the laser output. At $t \approx 8$ minutes (marked by the first orange line) the ethanol was poured into the Petri dish. The intensity decreases and the fluctuations increase dramatically. Ethanol does not absorb visible light, so this decrease in intensity is probably caused by scattering from the vapour. Ethanol evaporates and these vapours move above the Petri dish. The air with ethanol scatters the light in the cavity, decreasing the intensity of the recorded signal.

At the second orange line in the figure, a piece of cardboard was laid on top of the chimney. This effectively turns the volume above the Petri dish into a closed system and therefore prevents strong fluctuations in the vapour phase. When the volume is tightly closed, the vapour will

be saturated at some point. It is clear from the graph that closing the chimney with a piece of cardboard decreases the fluctuations in the measured intensity, and also that there is a decrease in intensity of approximately 2 % when the ethanol is poured into the Petri dish.

The vapour pressure of ethanol is 78.7 mbar, and using Equations 2.17 and 4.3, the cross section of ethanol is calculated to be $8.8 \cdot 10^{-28}\,\mathrm{m}^2$. The theory for Rayleigh scattering as set out in Equations 3.13 and 3.9 allows us to predict a theoretical value for the scattering cross section. The polarisability of ethanol[35] is $5.41 \cdot 10^{-30}\,\mathrm{m}^2$, yielding a theoretical cross section of $2.4 \cdot 10^{-30}\,\mathrm{m}^2$. The attenuation can therefore not be accounted for by only Rayleigh scattering and another contribution must exist. One possibility is that the rising vapours from the sample cause the vapour in the cavity to have a varying refractive index, therefore refracting the beam and decreasing the output from the cavity.

It is concluded that a volatile solvent can be detected by its scattering. The next step is to attempt to detect absorption at the laser wavelength by a dye in solution.

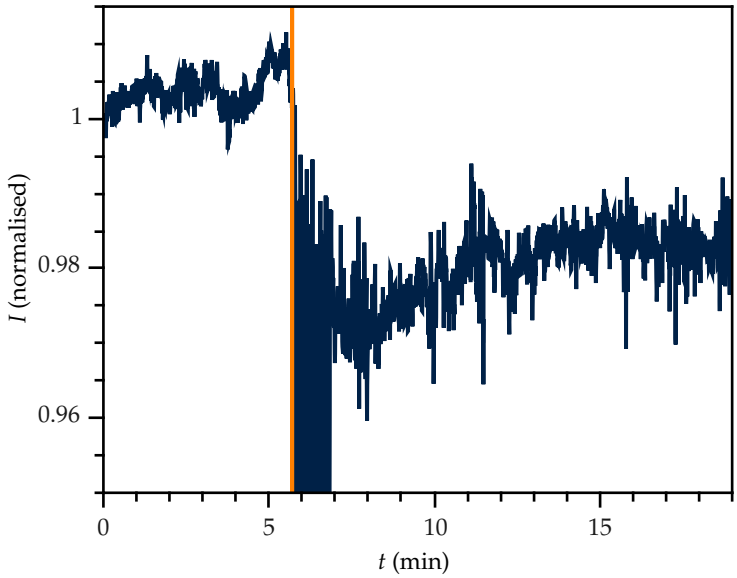

Figure 4.9: The CEAS signal recorded during the open air experiment with dye solution. At times to the left of the orange line the Petri dish is empty. After the orange line dye solution was poured into the Petri dish and a lid was laid on top of the chimney. The strongest fluctuations after the orange line originate from droplets blocking the beam in the cavity during the pouring of the dye solution.

Figure 4.9 shows a similar experiment, now performed using a $20\,\mathrm{g\,L}^{-1}$ guaiazulene solution in place of pure ethanol. At times to the left of the orange line in the figure, the Petri dish is empty, while after the orange line the dye solution was poured into the Petri dish. The strongest fluctuations are caused by droplets passing through the laser beam during the pouring of the dye solution and should therefore be ignored. The chimney was closed with a piece of cardboard. Again there is a decrease in intensity of 2 % visible, coming from the evaporation of ethanol. This

decrease is not measurably more than for the pure ethanol measurement, so there is no significant absorption observed for the dye in this experiment.

Since warming up the solution is expected to enhance evaporation of the dye, the experiment was repeated at a temperature of 60 °C. The result for pure ethanol is shown in Figure 4.10. At times to the left of the orange line the ethanol was present in the Petri dish with a lid on top at a temperature of 60 °C after equilibrating for half an hour. After the orange line the Petri dish is taken away from the cavity. It is clear from this figure that the presence of ethanol at 60 °C causes large fluctuations in the intensity, which was explained earlier. The fluctuations are much stronger than at room temperature, confirming that they are caused by the evaporation of ethanol.

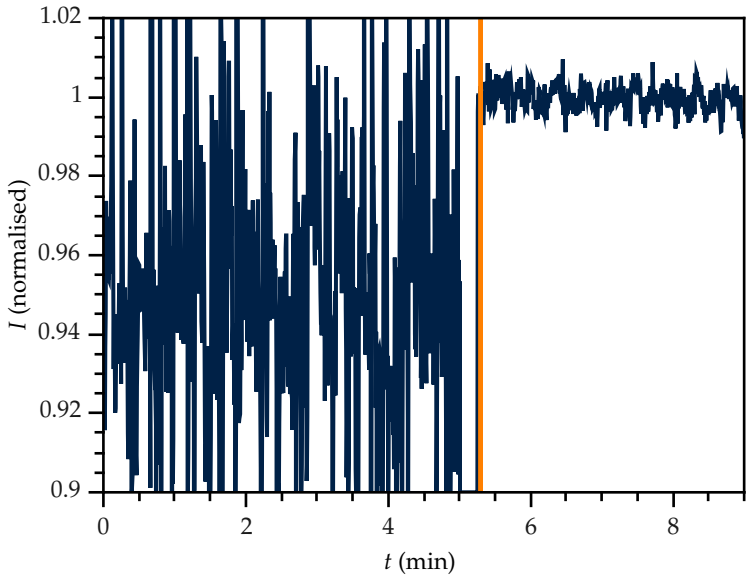

Figure 4.10: The CEAS signal recorded during a second open air experiment with dye solution. At times to the left of the orange line there is ethanol at 60 °C in the Petri dish. After the orange line the Petri dish was moved away from the cavity.

Figure 4.11 shows the same experiment, but now with a 20 g L^{-1} guaiazulene solution in ethanol. At times to the left of the orange line the sample is present after equilibrating for half an hour at 60 °C and after the orange line the Petri dish is taken away. As for the pure ethanol, for the solution the fluctuations increase dramatically at a higher temperature. However, there is no difference observed in comparison with the measurement of the pure ethanol. No measurable signal from the dye was observed.

The open air experiments were also repeated using potassium permanganate and sulforhodamine 101, using a CRDS instrument employing at 532 nm, see Section 3.3.3. The measurements were averaged over 406 ring-down traces, all of which were averaged over 512 laser shots. The result for the experiment was a ring-down time of 937.9±1.1 ns for an empty Petri dish. A ring-down time of 974 ns is expected using Equation 2.10. For a solution of 20 g L^{-1} potassium permanganate

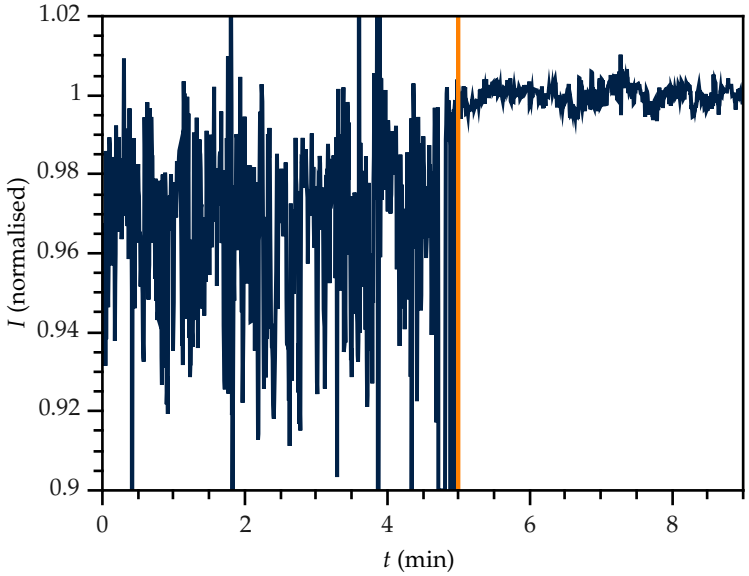

Figure 4.11: The CEAS signal recorded during the open air experiment with 20 g L^{-1} guaiazulene solution. At times to the left of the orange line there is a dye solution at 60 °C in the Petri dish. After the orange line the Petri dish was moved away from the cavity.

in water a ring-down time of 939.5±0.6 ns was observed and 937.0±0.7 ns for a solution of 1 g L^{-1} sulforhodamine 101 in water. No significant changes in the ring-down time were thus observed due to absorption by the dyes.

4.4.3 Vacuum chamber experiment

In Figure 4.12 the evolution of pressure in the vacuum system on exposure to a liquid sample is shown. The starting pressure of the system is 0.07 mbar, as discussed in Section 4.3.3. The figure shows that the pressure rises, but this increase slows down at higher pressures. This is explained by the vapour pressure of ethanol. When this pressure is reached, there is no longer a net flux of ethanol evaporation. The vapour pressure of ethanol at room temperature is 78.7 mbar. The pressure in the chamber after 24 hours reached approximately this value. The rate at which the pressure rises is directly related to the evaporation rate of ethanol, which becomes slower when the difference between the partial pressure of ethanol and the vapour pressure of ethanol decreases. A pressure evolution of the form $p = p_i\,(1 - \exp[-kt])$ is expected, in which p is the pressure and k is the evaporation rate constant.

The graph shows the pressure as a function of time after opening the valve to the sample for a sample of pure ethanol and for a solution of 20 g L^{-1} guaiazulene in ethanol. There is no significant difference between the two traces. This is as expected, since for low mole fractions of the dye in ethanol, the evaporative behaviour of ethanol is not expected to be influenced. Differences can be explained by inaccuracies associated with the readings from the analogue vacuum gauge.

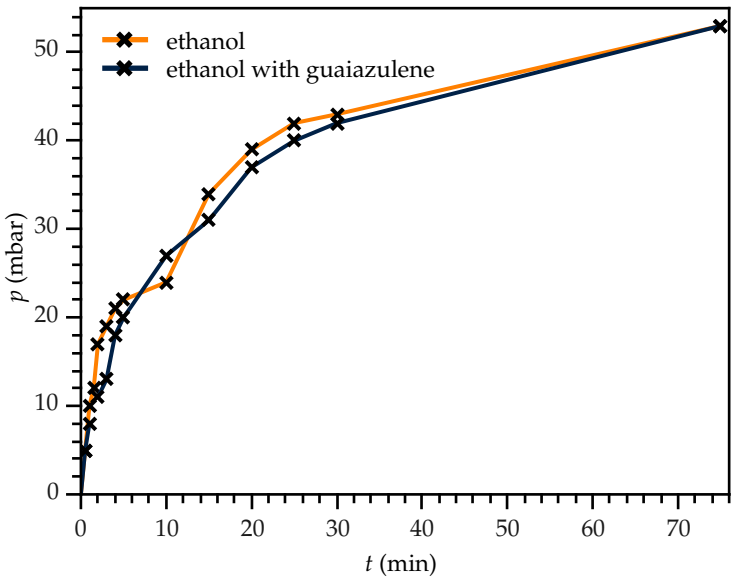

Figure 4.12: The evolution of the pressure in the vacuum chamber. The evaporation of ethanol causes the increase of the pressure up to its vapour pressure.

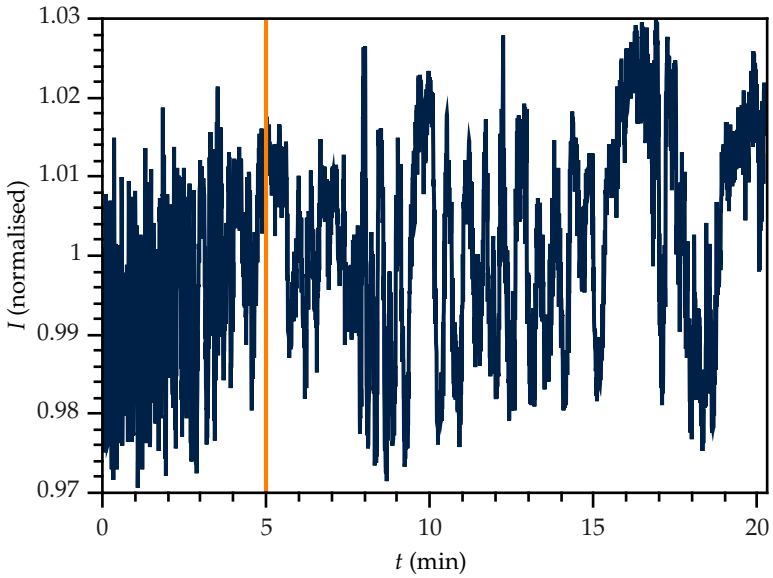

Figure 4.13: The CEAS signal recorded during the vacuum chamber experiment. At times to the left of the orange line, there was ethanol vapour possibly with some dye vapour, after 24 hours of equilibration. At the orange line any vapour was pumped out of the camber.

To investigate whether this setup could detect any of the guaiazulene dye in the vapour phase, the CEAS signal was monitored upon opening the valve to the sample holder. No change in

intensity with time was observed. A second attempt consisted of opening the valve for a time period of 24 hours to equilibrate. After this the vapour in the cavity was rapidly evacuated by pumping it out with the vacuum pump. Figure 4.13 shows the results of these measurements. At times to the left of the orange line a vapour of ethanol and possibly dye was present in the vacuum chamber, as a result of 24 hours of equilibration. After this time the vacuum pump was used to rapidly pump out the vapour. Since no change in intensity is observed, it can be concluded that there was not enough dye present to absorb the light in the cavity in a significant amount.

From this figure it also becomes clear that the ethanol is not detected. This supports the hypothesis that the attenuation in the open air experiment is not achieved by scattering, but by refraction by uncontrolled air flows above the Petri dish.

4.4.4 Theoretical consideration of the detection limit

The vapour pressure of guaiazulene is estimated to be $1.3 \cdot 10^{-3}$ mbar using the ACD/PhysChem Suite.[45] For a $20\,\mathrm{g\,L^{-1}}$ solution, the mole fraction is $1.8 \cdot 10^{-3}$. Using Equation 4.3, this results in a number density of $5.7 \cdot 10^{16}\,\mathrm{m^{-3}}$ of guaiazulene molecules in the vapour phase in equilibrium at room temperature. Using Equation 2.17, the expected change in cavity enhanced intensity for a cavity with $R = 0.99$ and $d = 585\,\mathrm{mm}$ is 0.05 %. This is much lower than what can be observed experimentally. Due to the fluctuations in the laser intensity, the lowest observable change is approximately 2 %.

Unfortunately, molecules that absorb light in the visible part of the spectrum accessible to our lasers, have in general a relatively high molecular mass. The result is that these molecules are not very volatile and that detection in the vapour phase is therefore difficult. Probing reactions of such molecules in solution by looking at the vapour phase is for this reason not a possibility, but there may be possibilities for probing more volatile species by their absorption in the infrared part of the spectrum.

For example, acetone has an absorption peak at $2\,970\,\mathrm{cm^{-1}}$ with a cross section[46] of $1.3 \cdot 10^{-23}\,\mathrm{m^2}$, and its vapour pressure at room temperature is 308 mbar.[35] For a CEAS experimental setup with $R = 0.99$ and $d = 585\,\mathrm{mm}$ and an experiment in which the mole fraction of acetone is 10^{-5}, this results in a decrease of 5 %, which is easily measured. An additional advantage is that gas-phase absorption lines in the infrared region are relatively narrow, and by choosing an appropriate wavelength this technique can therefore be made very specific to the analyte of interest.

Chapter 5

Conclusions

Two applications of cavity ring-down spectroscopy have been explored. First an evaporative light scattering detector was modified to incorporate detection by CRDS. The modification was carried out in such a way that the conventional light scattering detection system and CRDS could be used simultaneously. Experiments were performed to test whether the CRDS method would be more sensitive than the conventional method. It was shown that the CRDS detection method functions and gives qualitative results in agreement with the conventional measurements.

Quantitative results for the detector, including the results of calculations, are shown in Table 5.1.

Table 5.1: Overview of the measured and calculated detection limits.

method	detection limit (mg L^{-1})
conventional ELSD before modification	< 1
conventional ELSD after modification	5
CRDS measurements	1000
CRDS calculations	19

It is clear from these results that the ELSD is not more sensitive when employing the CRDS detection method. Even though the calculations show a much lower theoretically possible detection limit than the experimental value, this difference can perhaps be accounted for by diffusion of the solutes and the filtering of particles in the detector. The calculated detection limit for CRDS is much higher than the original limit of the detector.

Improvements of the CRDS measurements are possible, but calculations show that this will not result in more sensitive measurements than with the conventional ELSD. It is therefore concluded that CRDS can be used for ELSD, but that this will not result in significantly more sensitive measurements.

The second area in which CRDS detection was investigated was headspace analysis. Experiments employing solutions of the dye guaiazulene have shown that no dye can be detected in the headspace by using cavity enhanced absorption spectroscopy. Solutions of very high concentrations were used, without any resulting signal at all. The experiment was repeated by applying CRDS to the headspace of potassium permanganate and sulforhodamine 101, both giving no signal. For guaiazulene calculations have shown that in a thermodynamic equilibrium there will not be enough dye in the vapour phase to detect it with CRDS using our current setup, thus confirming the experimental data.

We conclude that headspace absorption spectroscopy with visible light is of limited use, since most molecules don't absorb in this region. Those who do absorb, are not very volatile. For example guaiazulene is a relatively volatile dye, the molecule is small for a typical molecule that absorbs in the visible part of the spectrum, and has a strong absorption, but nevertheless it could not be detected. It would be worthwhile to investigate headspace absorption spectroscopy in the infrared region of the spectrum, since nearly all organic molecules do absorb in this region. This possibility is discussed and a simple calculation has shown that experiments in this field may be successful.

References

1. A. O'Keefe and D. A. G. Deacon. Cavity ringdown optical spectrometer for absorption measurements using pulsed laser sources. *Rev. Sci. Instr.* **59**, 2544–2551 (1988).
2. P. Bouguer. *Essai d'optique, sur la gradation de la lumière* (Claude Jombert, 1729).
3. J. H. Lambert. *Photometria sive de mensura et gradibus luminis, colorum et umbrae* (Eberhardt Klett, 1760).
4. A. Beer. Bestimmung der Absorption des rothen Lichts in farbigen Flüssigkeiten. *Ann. Phys.* **162**, 78–88 (1852).
5. D. Romanini and K. K. Lehmann. Ringdown cavity absorption spectroscopy of the very weak HCN overtone bands with six, seven, and eight stretching quanta. *J. Chem. Phys.* **99**, 6387–6301 (1993).
6. C. Vallance. Innovations in cavity ringdown spectroscopy. *New J. Chem.* **29**, 867–874 (2005).
7. G. Berden and R. Engeln. *Cavity ring-down spectroscopy: techniques and applications* (Wiley, 2009), 1st edition.
8. C. C. Davis. *Lasers and electro-optics* (Cambridge University Press, 1996).
9. R. J. Pressley, ed. *CRC Handbook of lasers: with selected data on optical technology* (CRC Press, 1971).
10. M. S. Tswett. O novoy kategorii adsorbtsionnykh yavleny i o primenenii ikh k biokkhimicheskomu analizu. *Trudy Varhavskago Obshchestva Estestvoispytatelei, Otdelenie Biologii* **14**, 20–39 (1905).
11. L. S. Ettre. M.S. Tswett and the invention of chromatography. *LC-GC Eur.* **Sep 1**, 2–7 (2003).
12. R. P. W. Scott. *Liquid chromatography detectors* (Elsevier Science, 1977).
13. H. D. Young and R. A. Freedman. *University physics* (Pearson, 2008), 12th edition.
14. M. Swartz. HPLC detectors: a brief review. *J. Liq. Chrom. & Rel. Tech.* **33**, 1130–1150 (2010).
15. W. M. A. Niessen. *Liquid chromatography – mass spectrometry* (Taylor & Francis, 2006), 3rd edition.
16. D. L. Ford and W. Kennard. The evaporative analyzer. *J. Oil Colour Chem. Assoc.* **49**, 299–313 (1966).
17. M. Dreux, M. Lafosse and L. Morin-Allory. The evaporative light scattering detector – a universal instrument for non-volatile solutes in LC and SFC. *LC-GC Int.* **9**, 148–157 (1996).
18. N. C. Megoulas and M. A. Koupparis. Twenty years of evaporative light scattering detection.

Crit. Rev. Anal. Chem. **35**, 301–316 (2005).

19. S. Nukiyama and Y. Tanasawa. An experiment on the atomization of liquid by means of an air stream. *Trans. Jap. Soc. Mech. Eng.* **4**, 128–135 (1938).

20. L. B. Allen and J. A. Koropchak. Condensation nucleation light scattering: a new approach to development of high-sensitivity, universal detectors for separations. *Anal. Chem.* **65**, 841–844 (1993).

21. G. Guiochon, A. Moysan and C. Holley. Influence of various parameters on the response factors of the evaporative light scattering detector for a number of non-volatile compounds. *J. Liq. Chrom.* **11**, 2547–2570 (1988).

22. J. W. Strutt. On the light from the sky, its polarization and colour. *Phil. Mag.* **41**, 107–120 (1871).

23. G. Stokes. On the dynamical theory of diffraction. *Camb. Phil. Soc. Trans* **9**, 1–62 (1849).

24. H. C. van de Hulst. *Light scattering by small particles* (Dover Publications, 1981).

25. G. E. Thomas and K. Stamnes. *Radiative transfer in the atmosphere and ocean* (Cambridge University Press, 2002).

26. R. Loudon. *The quantum theory of light* (Oxford University Press, 2000), 3rd edition.

27. G. Mie. Beiträge zur Optik trüber Medien, speziell kolloidaler Metallösungen. *Ann. Phys.* **330**, 377–445 (1908).

28. W. J. Lentz. Generating Bessel functions in Mie scattering calculations using continued fractions. *Appl. Opt.* **3**, 668–671 (1976).

29. C. Mätzler. *MATLAB functions for Mie scattering and absorption*. Technical Report 2002-08, Institute of applied physics, University of Bern (2002).

30. R. O. Gumprecht and C. M. Sliepcevich. Scattering of light by large spherical particles. *J. Phys. Chem.* **57**, 90–95 (1953).

31. C. M. Rushworth, D. James, J. W. L. Lee and C. Vallance. Top notch design for fiber-loop cavity ring-down spectroscopy. *Anal. Chem.* **83**, 8492–8500 (2011).

32. I. M. J. J. van de Ven-Lucassen, F. G. Kieviet and P. J. A. M. Kerkhof. Fast and convenient implementation of the Taylor dispersion method. *J. Chem. Eng. Data* **40**, 407–411 (1995).

33. N. Lang-Yona, Y. Rudich, E. Segre, E. Dinar and A. Abo-Riziq. Complex refractive indices of aerosols retrieved by continuous wave-cavity ring down aerosol spectrometer. *Anal. Chem.* **81**, 1762–1769 (2009).

34. D. Mellon, S. J. King, J. Kim, J. P. Reid and A. J. Orr-Ewing. Measurements of extinction by aerosol particles in the near-infrared using continuous wave cavity ring-down spectroscopy. *J. Phys. Chem. A* **115**, 774–783 (2011).

35. D. R. Lide, ed. *Handbook of chemistry and physcis* (CRC Press, 2003), 84th edition.

36. D. James, B. Oag, C. M. Rushworth, J. W. L. Lee, J. Davies, J. T. Cabral and C. Vallance. High-sensitivity online detection for microfluidics via cavity ringdown spectroscopy. *RSC Adv.* (2012). In press.

37. K. L. Bechtel, R. N. Zare, A. A. Kachanov, S. S. Sanders and B. A. Paldus. Moving beyond traditional UV-Visible absorption detection: cavity ring-down spectroscopy for HPLC. *Anal. Chem.* **77**, 1177–1182 (2005).

38. L. van der Sneppen, F. Ariese, C. Gooijer and W. Ubachs. Liquid-phase and evanescent-wave cavity ring-down spectroscopy in analytical chemistry. *Annu. Rev. Anal. Chem.* **2**, 13–35 (2009).

39. B. Bahnev, L. van der Sneppen, A. E. Wiskerke, F. Ariese, C. Gooijer and W. Ubachs. Miniaturized cavity ring-down detection in a liquid flow cell. *Anal. Chem.* **77**, 1188–1191 (2005).

40. J. Wojtas, Z. Bielecki, T. Stacewicz, J. Mikołajczyk and M. Nowakowski. Ultrasensitive laser spectroscopy for breath analysis. *Opto-Electron. Rev.* **20**, 26–39 (2012).

41. M. Metsälä, F. M. Schmidt, M. Skyttä, O. Vaittinen and L. Halonen. Acetylene in breath: background levels and real-time elimination kinetics after smoking. *J. Breath. Res.* **4**, 046003 (2010).

42. B. Cummings, M. L. Hamilton, L. Ciaffoni, T. R. Pragnell, R. Peverall, G. A. D. Ritchie, G. Hancock and P. A. Robbins. Laser-based absorption spectroscopy as a technique for rapid in-line analysis of respired gas concentrations of O_2 and CO_2. *J. Appl. Physiol.* **111**, 303–307 (2011).

43. P. Atkins and J. de Paula. *Physical chemistry* (Oxford University Press, 2010), 9th edition.

44. J. R. Lakowicz. *Principles of fluorescence spectroscopy* (Springer, 2006), 3rd edition.

45. ACD/Labs (Retrieved: 29 May 2012). `http://www.acdlabs.com/`.

46. J. J. Harrison, N. D. C. Allen and P. F. Bernath. Infrared absorption cross sections for acetone (propanone) in the 3 μm region. *J. Quant. Spectrosc. & Radiat. Transfer* **112**, 53–58 (2011).

47. D. Marcuse. *Light transmission optics* (Van Nostrand Reinhold, 1972), 1st edition.

48. L. Råde and B. Westergren. *Mathematics handbook for science and engineering* (Birkhäuser, 1995), 1st edition.

49. J. Lekner. TM, TE and 'TEM' beam modes: exact solutions and their problems. *J. Opt. A: Pure Appl. Opt.* **3**, 407–412 (2001).

50. H. Kogelnik and T. Li. Laser beams and resonators. *Appl. Opt.* **5**, 1550–1567 (1966).

51. A. D. Polyanin and A. V. Manzhirov. *Handbook of mathematics for engineers and scientists* (Chapman & Hall/CRC, 2007), 1st edition.

Appendix A

Wave properties of light in a cavity

In general the amplitude of the electric field of an electromagnetic wave can be described by the Helmholtz equation, which is the time-independent form of the wave equation. The Helmholtz equation is[47]

$$\left(\nabla^2 + k^2\right) u = 0, \tag{A.1}$$

in which u is the amplitude of the electromagnetic field, k the wave number and ∇^2 the Laplace operator.

A.1 Paraxial approximation

Since cylindrical symmetry often appears in optical cavities, it is convenient to write the Laplace operator explicitly in cylindrical coordinates[48]

$$\frac{\partial^2 u}{\partial r^2} + \frac{1}{r}\frac{\partial u}{\partial r} + \frac{1}{r^2}\frac{\partial^2 u}{\partial \phi^2} + \frac{\partial^2 u}{\partial z^2} + k^2 u = 0. \tag{A.2}$$

This equation can be rewritten for a beam travelling along a straight line, for example the z-axis. In that case the main variation of the amplitude in the z-direction is contained in a factor $\mathrm{e}^{-\mathrm{i}kz}$, the description of a plane wave in the direction of z.[26] Then the amplitude is rewritten as

$$u = \psi\left(r, \phi, z\right) \cdot \mathrm{e}^{-\mathrm{i}kz}, \tag{A.3}$$

in which ψ is the difference between a plane wave travelling along the z-axis and the amplitude function describing a beam. When inserting this in Equation A.2, the required derivatives are

$$\frac{\partial u}{\partial r} = \mathrm{e}^{-\mathrm{i}\,kz} \cdot \frac{\partial \psi}{\partial r}; \tag{A.4}$$

$$\frac{\partial^2 u}{\partial r^2} = \mathrm{e}^{-\mathrm{i}\,kz} \cdot \frac{\partial^2 \psi}{\partial r^2}; \tag{A.5}$$

$$\frac{\partial^2 u}{\partial \phi^2} = \mathrm{e}^{-\mathrm{i}\,kz} \cdot \frac{\partial^2 \psi}{\partial \phi^2}; \tag{A.6}$$

$$\frac{\partial^2 u}{\partial z^2} = \mathrm{e}^{-\mathrm{i}\,kz} \cdot \left(\frac{\partial^2 \psi}{\partial z^2} - 2\,\mathrm{i}\,k \frac{\partial \psi}{\partial z} - k^2 \psi \right). \tag{A.7}$$

Equation A.2 is then reduced to

$$\frac{\partial^2 \psi}{\partial r^2} + \frac{1}{r}\frac{\partial \psi}{\partial r} + \frac{1}{r^2}\frac{\partial^2 \psi}{\partial \phi^2} - 2\,\mathrm{i}\,k \frac{\partial \psi}{\partial z} + \frac{\partial^2 \psi}{\partial z^2} = 0. \tag{A.8}$$

Since it was assumed that the main variation of the beam in the z-direction was contained in the factor $\mathrm{e}^{-\mathrm{i}\,kz}$, the term $\frac{\partial^2 \psi}{\partial z^2}$ is negligible compared to $k\frac{\partial \psi}{\partial z}$. The Helmholtz equation is then written in terms of an expression known as the paraxial approximation[49]

$$\frac{\partial^2 \psi}{\partial r^2} + \frac{1}{r}\frac{\partial \psi}{\partial r} + \frac{1}{r^2}\frac{\partial^2 \psi}{\partial \phi^2} - 2\,\mathrm{i}\,k \frac{\partial \psi}{\partial z} = 0. \tag{A.9}$$

A.2 Fundamental Gaussian beam

To obtain the shape and phase of a light beam, Equation A.9, a partial differential equation, has to be solved. This can be done by trying a solution of the form[8]

$$\psi(r, z) = \exp\left[-\mathrm{i} \left(\Phi(z) + \frac{k r^2}{2\,q(z)} \right) \right], \tag{A.10}$$

in which $\Phi(z)$ is a phase shift factor, a complex quantity, and $q(z)$ is the complex beam parameter. In order to substitute the proposed solution into Equation A.9, the required derivatives are

$$\frac{\partial \psi}{\partial r} = -\psi \frac{\mathrm{i}\,kr}{q(z)}; \tag{A.11}$$

$$\frac{\partial^2\psi}{\partial r^2} = \psi\left(-\frac{k^2 r^2}{q^2(z)} - \frac{\mathrm{i}\,k}{q(z)}\right); \tag{A.12}$$

$$\frac{\partial^2\psi}{\partial \phi^2} = 0; \tag{A.13}$$

$$\frac{\partial\psi}{\partial z} = \psi\left(\frac{\mathrm{i}\,k r^2}{2\,q^2(z)}\frac{\partial q(z)}{\partial z} - \mathrm{i}\frac{\partial\,\Phi(z)}{\partial z}\right). \tag{A.14}$$

Using these derivatives, the resulting equation is

$$\frac{k^2 r^2}{q^2(z)}\left(\frac{\partial q(z)}{\partial z} - 1\right) - 2\,k\frac{\partial\,\Phi(z)}{\partial z} - \frac{2\,\mathrm{i}\,k}{q(z)} = 0. \tag{A.15}$$

Since the equation must be valid for any value of r, it can be separated into the two simple differential equations

$$\frac{\mathrm{d}q(z)}{\mathrm{d}z} = 1 \tag{A.16}$$

and

$$\frac{\mathrm{d}\Phi(z)}{\mathrm{d}z} = -\frac{\mathrm{i}}{q(z)}. \tag{A.17}$$

The solution to the first differential equation is

$$q(z) = z + q(0). \tag{A.18}$$

For convenience it is defined that at $z = 0$ the beam is a plane wave

$$R(0) = \infty. \tag{A.19}$$

The complex beam parameter then reduces at $z = 0$ to

$$\frac{1}{q(0)} = -\frac{2\,\mathrm{i}}{k\,w^2(0)}, \tag{A.20}$$

which can be used together with Equation A.18 to obtain an expression for $w(z)$

$$q(z) = z + \frac{\mathrm{i}\, k\, w^2(0)}{2}. \tag{A.21}$$

This result and Equation 2.18 combine to

$$\frac{1}{q(z)} = \frac{1}{q(0) + z} \tag{A.22}$$

$$\frac{1}{R} - \frac{2\,\mathrm{i}}{k\, w^2(z)} = \frac{1}{\frac{\mathrm{i}\, k\, w^2(0)}{2} + z} = \frac{z - \frac{\mathrm{i}\, k\, w^2(0)}{2}}{\frac{k^2\, w^4(0)}{4} + z^2}. \tag{A.23}$$

Equating the imaginary parts results in

$$\frac{2}{k\, w^2(z)} = \frac{\frac{k\, w^2(0)}{2}}{\frac{k^2\, w^4(0)}{4} + z^2}, \tag{A.24}$$

which results after some rearrangements in ‡

$$w^2(z) = w^2(0)\left(1 + \left(\frac{2z}{k\, w^2(0)}\right)^2\right). \tag{A.25}$$

The beam is at its narrowest at $z = 0$, thus this is called the beam waist.

Now an expression for $\Phi(z)$ can be derived. With Equation A.18, we can rewrite Equation A.17 to

$$\frac{\partial\, \Phi(z)}{\partial z} = -\frac{\mathrm{i}}{z + q(0)}, \tag{A.26}$$

---

‡ Equation A.25 also shows why a beam cannot be perfectly collimated over a long distance. When z is large, the equation is approximately

$$w(z) \approx \frac{2z}{k\, w(0)}.$$

The radial divergence of a beam is then

$$\theta = \arctan\left[\frac{w(z)}{z}\right] \approx \frac{w(z)}{z} = \frac{2}{k\, w(0)}.$$

According to this equation, θ cannot be zero, thus a beam cannot be perfectly collimated. A wide beam, $w(0)$ is large, can be less divergent than a narrow beam, $w(0)$ is small. When the divergence of a beam fulfils the equation above, it has reached the lowest possible divergence and is then said to be diffraction limited.

which solves to

$$\Phi(z) = -\mathrm{i}\ln\left[z + q(0)\right] + C = -\mathrm{i}\ln\left[z + \frac{\mathrm{i}\,k\,w^2(0)}{2}\right] + C. \tag{A.27}$$

In this equation is C the integration constant. The integration constant can have any value, since the phase of a wave is only determined relative to another phase. It is chosen in such a way that $\Phi(0) = 0$

$$C = -\mathrm{i}\ln\left[\frac{2}{\mathrm{i}\,k\,w^2(0)}\right]. \tag{A.28}$$

When the resulting complex term within the natural logarithm of Φ is written in exponential form, it can be split in a real and imaginary part

$$\begin{aligned}
\Phi(z) &= -\mathrm{i}\left(\ln\left[z + \frac{\mathrm{i}\,k\,w^2(0)}{2}\right] + \ln\left[\frac{2}{\mathrm{i}\,k\,w^2(0)}\right]\right) = -\mathrm{i}\ln\left[1 - \frac{2\,\mathrm{i}\,z}{k\,w^2(0)}\right] \\
&= -\mathrm{i}\ln\left[\sqrt{1 + \left(\frac{2z}{k\,w^2(0)}\right)^2}\cdot\exp\left[\mathrm{i}\arctan\left[-\frac{2z}{k\,w^2(0)}\right]\right]\right] \\
&= \arctan\left[-\frac{2z}{k\,w^2(0)}\right] + \mathrm{i}\ln\left[\frac{w(0)}{w(z)}\right].
\end{aligned} \tag{A.29}$$

By substituting Equations 2.18 and A.29 in Equation A.10, the final result is ‡

$$\psi(r,z) = \frac{w(0)}{w(z)}\exp\left[-\frac{r^2}{w^2(z)}\right]\exp\left[-\frac{\mathrm{i}\,kr^2}{2R(z)}\right]\exp\left[\mathrm{i}\,\zeta(z)\right], \tag{A.30}$$

in which $\zeta = \arctan\left[\frac{2z}{k\,w^2(0)}\right]$. The intensity is equal to the absolute square of the amplitude

‡ Equation A.30 can be used to show the physical meaning of R(z). Using Equation A.3, it is seen that the total phase of the amplitude function is

$$-\frac{kr^2}{2R(z)} + \arctan\left[\frac{2z}{k\,w^2(0)}\right] - kz.$$

For large z (and this is often the case), the term with the arc tangent approaches a constant, $\frac{\pi}{2}$. When the wavefront is to be found, it is needed to search for all the points with the same phase, so the restriction is

$$z = C - \frac{r^2}{2R(z)}$$

The constant C includes here k and the value of $\frac{\pi}{2}$. This is a parabola, which for $r \ll z$ (which is mostly the case for a light beam) can be approximated by a circle. This is visible by writing the equation for z as a function of r in case of a circle with radius R (a series expansion is used)

$$z = \sqrt{R^2 - r^2} = R\sqrt{1 - \frac{r^2}{R^2}} \approx R\left(1 - \frac{r^2}{2R^2}\right) = C' - \frac{r^2}{2R}.$$

It is clear now that there is a spherical wavefront and that $R(z)$ can be interpreted as the radius of curvature of the wavefront.

function[43]

$$I(r,z) = uu^* = \psi\psi^* = \left(\frac{w(0)}{w(z)}\right)^2 \exp\left[-\frac{2r^2}{w^2(z)}\right]. \tag{A.31}$$

This is a Gaussian distribution as a function of the distance from the propagation axis and therefore this solution is called a fundamental Gaussian beam. It is now clear that $w(z)$ is a measure for the width of the Gaussian beam. A cross section of such a beam for a chosen $w(0)$ and $w(z)$ is shown in Figure A.1.

Figure A.1: The beam intensity of a cross section of a fundamental Gaussian beam for a chosen $w(0)$ and $w(z)$.

A.3 Higher order modes

The fundamental Gaussian beam is one possible solution to the paraxial approximation, but not the only possible solution. More general solutions may include radial and angular nodes, thus a proposed (more general) solution for Equation A.9 may be the fundamental Gaussian beam with radial and angular nodes incorporated[50]

$$\psi\left(r,\phi,z\right) = f\Big(r,w(z)\Big)\cdot\psi\left(r,z\right)\begin{Bmatrix}\sin\left[l\phi\right]\\ \cos\left[l\phi\right]\end{Bmatrix}, \tag{A.32}$$

where l is an integer and $f\Big(r,w(z)\Big)$ can be any function. Both a function with a sine or cosine is possible. The general solution to the paraxial differential equation is[50]

$$\psi_{ml}\left(r,\phi,z\right) = \left(\sqrt{2}\frac{r}{w(z)}\right)^l L_m^l\left(\frac{2r^2}{w^2(z)}\right)\begin{Bmatrix}\sin\left[l\phi\right]\\ \cos\left[l\phi\right]\end{Bmatrix}\exp\left[-\frac{r^2}{w^2(z)}\right]\exp\left[\frac{\mathrm{i}\,kr^2}{2R(z)}\right]\exp\Big[-\mathrm{i}\,(2m+l+1)\,\zeta(z)\Big]. \tag{A.33}$$

In this equation are L_m^l the associated Laguerre polynomials[48]

$$L_m^l(x) = \frac{e^x x^{-l}}{m!}\frac{d^m}{dx^m}\left(e^{-x}x^{m+l}\right) = \frac{1}{m!}\sum_{i=0}^{n}\frac{m!}{i!}\binom{m+l}{m-i}(-x)^i, \tag{A.34}$$

which are solutions to the associated Laguerre differential equation

$$x\frac{d^2L_m^l(x)}{dx^2} + (l+1-x)\frac{dL_m^l(x)}{dx} + m\,L_m^l(x) = 0. \tag{A.35}$$

Since the main difference with the fundamental Gaussian beam is the distribution in the transverse plane, the plane perpendicular to the direction of propagation, these solutions of the paraxial approximation are called transverse modes. Equation A.33 is one complete set of possible solutions. However, other sets which are for example more convenient for cavities with a different symmetry can also be derived. The transverse modes are often referred to as TEM_{ml} (Transverse Electric and Magnetic) modes, where m and l are the radial and angular number of nodes, which are parameters as seen in the equation for ψ_{ml}. Another notation is LG_{ml} where LG stands for Laguerre-Gaussian. This in contrast with for example HG_{mn}, which are the Hermite-Gaussian solutions, suitable when the cavity has the transverse shape of a rectangle. In either case TEM_{00} (or LG_{00} or HG_{00}) refers to the fundamental Gaussian beam. The intensity is obtained from the absolute square of the amplitude function

$$I_{ml}\left(r,\phi,z\right) = uu^* = \psi\psi^* = \left(\frac{2r^2}{w^2(z)}\right)^l\left(L_m^l\left(\frac{2r^2}{w^2(z)}\right)\begin{Bmatrix}\sin\left[l\phi\right]\\ \cos\left[l\phi\right]\end{Bmatrix}\right)^2\exp\left[-\frac{2r^2}{w^2(z)}\right] \tag{A.36}$$

and the intensity patterns for a chosen $w(z)$ are shown in Figure A.2. The radial and angular modes are clearly visible and it becomes clear that the mode for $m = 0$ and $l = 0$ is the fundamental Gaussian beam.

Depending on the application, it may be preferred that only the fundamental Gaussian beam is supported by the cavity. As can be seen in the figure the higher order transverse modes spread out more and collection of the signal at the back mirror will then be more complicated. A well aligned cavity will mainly support fundamental Gaussian beams and during the alignment of the cavity the shapes of (linear combinations of) the transverse modes can be visualised by placing a screen or camera behind the back mirror.

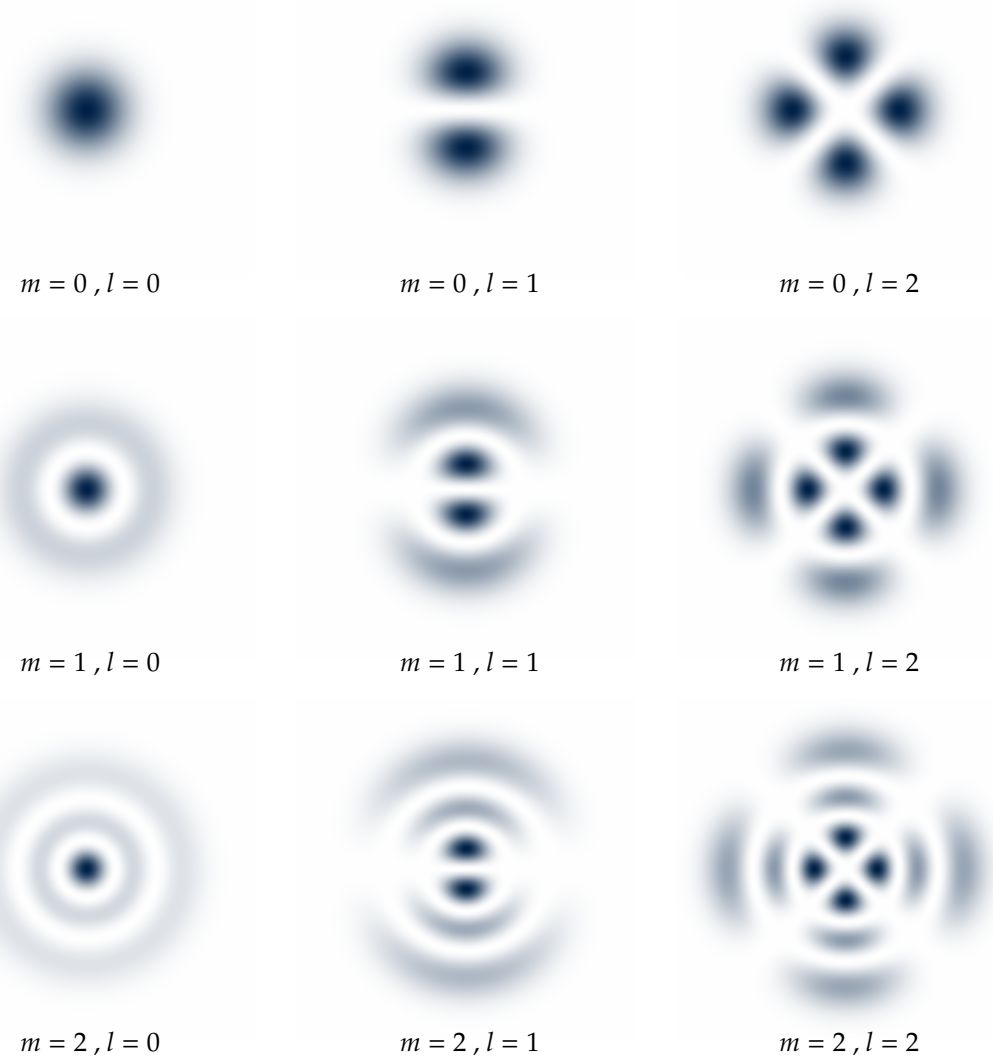

Figure A.2: The transverse modes of a cavity with cylindrical symmetry. Equation A.36, in this case using the cosine, describes these patterns. It is clearly visible in these figures that m corresponds to the number of radial nodes, while l corresponds to the number of angular modes.

A.4 Stable mode frequencies in cavity

The Laguerre-Gaussian modes describe possible solutions of the Helmholtz equation of a light beam in the paraxial approximation. It does not impose any boundary conditions on the system though and therefore not all modes with all possible wave numbers may be supported by a specific cavity when the boundary conditions are taken into account.

The total phase in the Laguerre-Gaussian modes at $r = 0$ can be read from Equations A.33 and A.3

$$- \; kz - (2m + l + 1) \arctan\left[\frac{2z}{k\, w^2(0)}\right]. \tag{A.37}$$

The cavity will support a standing wave when at a mirror the reflected wave is in phase with the incoming wave, which gives the condition that the length L of the cavity should be an integer or half-integer number of wavelengths. This is equivalent to the requirement that after travelling from one mirror to the other the phase has changed by an integer times π.[50] When the middle of a symmetrical cavity with length L is defined as $z = 0$, then the phase of the beam at one mirror is

$$\frac{kL}{2} - (2m + l + 1) \arctan\left[-\frac{L}{k\, w^2(0)}\right] \tag{A.38}$$

and at the other mirror

$$-\frac{kL}{2} - (2m + l + 1) \arctan\left[\frac{L}{k\, w^2(0)}\right]. \tag{A.39}$$

The difference between these two phases should be equal to an integer times π

$$kL + 2\ (2m + l + 1) \arctan\left[\frac{L}{k\, w^2(0)}\right] = o\pi, \tag{A.40}$$

in which o is an integer. Using $k = \frac{2\pi\nu}{c}$, the result is

$$\nu_{mlo} = \frac{c}{2L}\left(m + 2\,\frac{2m + l + 1}{\pi} \arctan\left[\frac{L}{k\, w^2(0)}\right]\right). \tag{A.41}$$

It can be useful to write the term in the arc tangent as a function of variables which are determined more easily in the experimental setup than the beam waist size. For that it will be needed to derive an expression for the beam waist size in the cavity. For practical purposes a symmetrical cavity is assumed, thus having two concave mirrors with the same radius of curvature. Using Equations 2.18 and 2.23 and recognising that both k and $w(z)$ are positive quantities, Equation 2.27 reduces in this situation to

$$\frac{1}{q} = \frac{1}{R} - \mathrm{i}\sqrt{\frac{2}{RL} - \frac{1}{R^2}}. \tag{A.42}$$

Using Equations A.20, A.18 and the previous equation, the expression for the beam waist size is

$$w^2(0) = \frac{2\,q(0)}{\mathrm{i}\,k} = \frac{2\left(q(z)+z\right)}{\mathrm{i}\,k} = \frac{2}{\mathrm{i}\,k}\left(\frac{1}{\frac{1}{R} - \mathrm{i}\sqrt{\frac{2}{RL} - \frac{1}{R^2}}} + z\right) = \frac{2}{\mathrm{i}\,k}\left(\frac{\frac{1}{R} + \mathrm{i}\sqrt{\frac{2}{RL} - \frac{1}{R^2}}}{\frac{1}{R^2} + \left(\frac{2}{RL} - \frac{1}{R^2}\right)} + z\right). \tag{A.43}$$

Since $w(0)$ is a real quantity, the imaginary parts of the right hand side can be taken out

$$\frac{k\,w^2(0)}{L} = R\sqrt{\frac{2}{RL} - \frac{1}{R^2}} = \sqrt{\frac{2R}{L} - 1}. \tag{A.44}$$

Using this result, Equation A.41 is then rewritten as

$$\nu_{mlo} = \frac{c}{2L}\left(o + 2\,\frac{2m+l+1}{\pi}\arctan\left[\frac{1}{\sqrt{\frac{2R}{L} - 1}}\right]\right). \tag{A.45}$$

The trigonometric relations[51]

$$\arccos x = \arctan\left[\frac{\sqrt{1-x^2}}{x}\right] \tag{A.46}$$

and

$$\arctan x + \arctan y = \arctan\left[\frac{xy}{1-xy}\right] \tag{A.47}$$

can be used to write

$$\arccos x = 2\arctan\left[\frac{\sqrt{1-x^2}}{1+x}\right] \tag{A.48}$$

and if $\frac{1}{\sqrt{\frac{2R}{L}-1}}$ is expressed as $\frac{\sqrt{1-\left(1-\frac{L}{R}\right)^2}}{1+\left(1-\frac{L}{R}\right)}$, this simplifies Equation A.45 to an expression in experimental parameters which are easily determined

$$\nu_{mlo} = \frac{c}{2L}\left(o + \frac{2m+l+1}{\pi}\arccos\left[1 - \frac{L}{R}\right]\right). \tag{A.49}$$

This equation is a very important result. At first it shows that after following a derivation which takes into account the wave character of the light, standing waves are supported by an optical

cavity. Next to that it shows that the waves supported by an optical cavity are quantised: for a given mode, only specific wavelengths can survive in the optical cavity. This is relevant both when exciting a cavity, as well as detecting the output. For CRDS it means that only specific wavelengths will undergo ring-down events and that only species attenuating the light at these wavelengths are detected. The equation also gives the possibility of calculating these supported frequencies and it shows how the separation between these depends on the length of the cavity (a longer cavity corresponds to more closely spaced supported frequencies).